

INVESTIGATION OF  
TERAHERTZ TECHNOLOGY  
AND APPLICATIONS

by

JUHYUNG KIM

SEONGSIN M. KIM, COMMITTEE CHAIR  
PATRICK KUNG  
CHARLES O'NEILL

A THESIS

Submitted in partial fulfillment of the requirements  
for the degree of Master of Science  
in the Department of Electrical and Computer Engineering  
in the Graduate School of  
The University of Alabama

TUSCALOOSA, ALABAMA

2015

Copyright Juhyung Kim 2015

ALL RIGHTS RESERVED

## ABSTRACT

Terahertz Technology promises significant advancement in various field including military applications, biomedical industry and future communication as a convergence area between electronics fields and photonics fields. In this thesis, I present the development of Terahertz technology based on Terahertz Time Domain Spectroscopy and its methodologies that I had to learn to utilize the system and to improve the quality of data acquired.

After the methodology is presented, there are three main topics investigated for the Terahertz technology applications. First, Flexible Metamaterial Perfect Absorber was fabricated and investigated as a new Terahertz responsive device. Second, human breast tissue cell lines and cancer cell lines are distinguished by analyzing spectroscopic data gotten from transmission mode of Terahertz Time-domain Spectroscopy. Third, after testing the Terahertz wave radiation from SiGe nanowires surface emitter, InP and InGaAs nanowires were tested as an alternative material. Especially, those were fabricated with a new trial of fabrication, the E-beam lithography, to obtain a regular vertical alignment and uniform distribution with desired diameter and length, instead of randomly grown nanowires. Polarization dependent measurement result will be demonstrated depending on the size and shape of these nanowires.

## DEDICATION

This thesis is dedicated to the Republic of Korea Navy and everyone who helped and guided me through the trials and tribulations of creating this manuscript. In particular, my wife Karen who stood by me throughout the time it took me to complete this thesis.

## LIST OF ABBREVIATIONS AND SYMBOLS

<i>BS</i>	Beam Splitter
<i>CMCs</i>	Ceramic Metal Composite materials
<i>CW</i>	Continuous Wave
<i>DFT</i>	discrete Fourier transform
<i>DMEM</i>	Dulbecco's Modified Eagle's Medium
<i>E-Beam</i>	electron beam
<i>FFT</i>	Fast Fourier Transform
<i>FMPA</i>	Flexible metamaterial perfect absorbers
<i>FSS</i>	Frequency Selective Surface
<i>FBS</i>	Fetal Bovine Serum
<i>GHz</i>	Gigahertz
<i>HSQ</i>	Hydrogen silsesquioxane
<i>HWP</i>	Half Wave Plate
<i>LT-GaAs</i>	Low-temperature grown Gallium Arsenide
<i>MBE</i>	molecular beam epitaxy
<i>MEBM</i>	Mammary Epithelial Basal Medium
<i>meV</i>	milli electron Volt
<i>MHz</i>	Megahertz

<i>MMCs</i>	Metal Matrix Composite materials
<i>NW</i>	<i>Nanowire</i>
<i>Nd: YVO<sub>4</sub></i>	Neodymium doped yttrium orthovanadate
<i>OAP</i>	Off-axis parabolic
<i>PCA</i>	Photo Conductive Antenna
<i>PDMS</i>	Polydimethylsiloxane
<i>PMCs</i>	Polymer Matrix Composite materials
<i>QWP</i>	Quarter Wave Plate
<i>RCS</i>	Radar Cross Section
<i>RF</i>	Radio Frequency
<i>Si</i>	Silicon
<i>THz</i>	Terahertz
<i>TDS</i>	Time Domain Spectroscopy
<i>Ti: S</i>	Titanium: Sapphire
<i>TIR</i>	Total internal reflection
=	equal to
$\Sigma$	Sigma

## ACKNOWLEDGEMENTS

I am pleased to have this opportunity to thank the many colleagues, friends, and faculty members who have helped me with this research project. I am most indebted to Dr. Seongsin Margaret Kim, the chairman of this thesis, for sharing her research expertise and wisdom regarding motivational theory. I would also like to thank all of my committee members, Dr. Patrick Kung and Dr. Charles O'Neill for their invaluable input, inspiring questions, and support of both the thesis and my academic progress.

Especially, this research would not have been possible without the support of my friends and fellow graduate students and of course of my wife Karen who never stopped encouraging me to persist. I would like to thank Soner Balci and Mohammad Parvinezhad Hokmabadi for their strong assistance and mental support whenever I was in difficult condition.

Most of all, I gratefully acknowledge financial support from the Republic of Korea Navy for giving me an opportunity to acquire Master's degree here in the United States.

## CONTENTS

ABSTRACT .....	ii
DEDICATION .....	iii
LIST OF ABBREVIATIONS AND SYMBOLS .....	iv
ACKNOWLEDGEMENTS .....	vi
LIST OF TABLES .....	x
LIST OF FIGURES .....	xi
1. INTRODUCTION .....	1
1.1. Overview of the Thesis .....	1
1.2. THz Technology Review .....	3
1.3. Characteristic, Pros & Cons and applications of THz Wave .....	6
2. METHODOLOGY .....	8
2.1. Techniques for investigation of THz wave .....	8
2.2. THz-Time Domain Spectroscopy .....	12
2.2.1. System Introduction .....	12
2.2.2. TDS System .....	13
2.3. System Configuration and Optics Alignment .....	15
2.3.1. Generating Stable Laser Pulse (Mode-Locking) .....	15
2.3.2. Software Development for Verdi Control and Mode-Lock .....	16

2.3.3. Experimental Mode Transform and Optics Re-alignment...	26
2.4. Data Processing.....	27
2.4.1. THz Waveform Acquisition and Conversion.....	27
2.4.2. Extracting Information and Improving of Signal Quality ....	29
2.5. THz Imaging.....	32
3. FLEXIBLE METAMATERIAL PERFECT ABSORBERS .....	36
3.1. Introduction .....	36
3.2. Design and Simulation .....	39
3.3. Experimental Procedure .....	42
3.4. Results and Discussion.....	44
3.5. Summary .....	49
4. INVESTIGATION OF BREAST EPITHELIAL LINE USING THZ-TDS .....	50
4.1. Introduction .....	50
4.2. Experimental procedure .....	52
4.2.1. Sample Culturing.....	52
4.2.2. Measurement preparation.....	53
4.3. Result.....	54
4.4. Summary .....	57
5. THZ EMISSION FROM NANOWIRES .....	58
5.1. Introduction .....	58
5.2. Experiment procedure .....	59
5.2.1. Measurement Setup.....	59
5.2.2. Sample Fabrication.....	61

5.3. Results and Discussion.....	62
5.4. Summary .....	65
6. CONCLUSION.....	66
REFERENCES .....	68

## LIST OF TABLES

1.1 Comparison of Electronics and Photonics (optics).....	4
2.1 The absorption lines in the THz-TDS spectral range due to atmospheric water vapor .....	31
3.1 Dimensions of bottom ring and top ring with respect to the displacement of the structures .....	40

## LIST OF FIGURES

1.1 The Terahertz band in the electromagnetic spectrum.....	3
1.2 Electronics and Photonics industrial convergence.....	5
2.1 Diagram of typical PCA generation mechanism and principle of THz emission from PCA.....	10
2.2 Scheme of Electro-Optical Sampling.....	11
2.3 Diagram of Laser Pulse Generation and the THz-TDS system .....	13
1.4 The principle of the emission and detection of THz in TDS .....	14
2.5 Picture of MIRA900B and optical schematic diagram inside .....	15
2.6 Schematic representation of the set up to be monitored .....	17
2.7 Picture of set-up, mode-locked and non-mode-locked signals displayed by digital oscilloscope.....	18
2.8 The front panel of the main VI with stop point is equal to 1000 and user tab view, with stop point is equal to 300 and advanced tab view.....	19
2.9 Block diagram of main VI including two sequences for default settings and event structure inside a while loop.....	20
2.10 The front panel and block diagram of basic ‘ReadWriteQuery’ SubVI .....	20
2.11 Illustration of four major parts of timeout event.....	22
2.12 Block diagram of ‘ASCII Format Data Acquisition’ SubVI .....	22
2.13 Block diagram of ‘Binary Format Data Acquisition’ SubVI.....	23
2.14 Close view of Mode Lock Check and Operation category of timeout .....	24
2.15 Block diagram of ‘Mode Lock Status’ SubVI .....	24
2.16 Block diagram of ‘Statistics Reset Needed’ SubVI.....	25

2.17 Block diagram of ‘Mode Lock Lost Action’ SubVI.....	25
2.18 Diagram of the transmission mode and reflection mode scheme .....	26
2.19 Typical time domain THz pulse in the air and its transformation into frequency domain data.....	29
2.20 Frequency spectrum comparison of raw data and processed data after removing the etalon effect from the time-domain waveform.....	30
2.21 Power spectra comparison between before and after purging with N <sub>2</sub> .....	32
2.22 Picture of 3-axis motion control stage .....	32
2.23 Procedure finding the beam position in terms of 3-axis values by performing first scan with maximum (20x20mm) window and second scan with smaller (4x4mm) window.....	33
2.24 Multiple slides obtained by fast mode THz imaging by moving y-axis after building up x-z plane. The white circle at center slightly moves along the y-axis.....	34
2.25 Description of fast scan mode and regular scan mode.....	34
2.26 THz imaging test of a piece of real organic branch and its imaging result when hidden in a paper box .....	35
3.1 Principle of carbon fiber composites as an example of RAM .....	38
3.2 Diagrams of the top view of the FSS layer consisting of two non-concentric rings with labeled incident field polarizations, side view, and center-to- center displacement ring geometries of the flexible absorber unit cell .....	40
3.3 Simulated absorbance of the FMPAs at 0° and 90° at varied center-to-center ring displacements given.....	41
3.4 Optical microscope picture of fabricated FMPA with 8μm center-to-center displacement and Diagrams of the deformation vacuum holder design with device conformation to the cylindrical and spherical surface relief structures.....	44
3.5 Simulated and measured absorbance of the FMPAs for fixed one on a parental Si wafer when the center-to-center ring displacements was 6μm and 8μm, and measured change in resonant frequency as a function of center-to-center ring displacement at 0° E-field polarization.....	45

3.6 Measured and simulated absorbance of the FMPAs on a flat surface at 0° and 90° at varied center-to-center ring displacements.....	46
3.7 Pictures of deformed flexible device on a cylindrical, hemispherical, pyramid shape of custom holders by using vacuum force.....	46
3.8 Measured absorbance of the FMPA on a various type of surface at 0° E-field polarization .....	47
3.9 Absorbance at resonant frequency as a function of shape in 0° and 90° .....	48
4.1 Microscopic Images of the MDA-MB-231 Cancer cells in the growth media DMEM and 184A1 Normal cells in the growth media MEBM.....	52
4.2 Diagram of Transmission mode TDS and the pictures of the sample stages...	53
4.3 Transmission ratio of the both media for cancer cells and normal cells as a negative control measurement .....	54
4.4 Measurement result of cancer cell line and normal cell line in purged and non-sealed condition .....	55
4.5 Measurement result of cancer cell line and normal cell line in purged and sealed condition .....	56
4.6 Difference in transmission ratio of living cells and dead cells using THz-TDS spectroscopy.....	57
5.1 Diagram of setup for THz emission test from NWs .....	60
5.2 SEM images of the Si1-xGex nanowire samples and its composition ratios ..	61
5.3 Low-magnification SEM image of the InP nanowire arrays showing the perfect uniform distribution of the wires with a 2µm of fixed pitch length. Higher-magnification SEM image which shows the dimension of each NWs. Low-magnification SEM image of the InGaAs nanowire arrays. Higher-magnification SEM image of InGaAs which shows the dimension of each NWs.....	62
5.4 Measurement in time-domain graph comparing the THz amplitude detected by different combination of SiGe NWs and comparison of peak to peak value for the measured time-domain signals .....	62
5.5 Overlapped amplitudes of emitted THz from InP/InGaAs NWs and their parental wafers .....	63

5.6 THz emission from fabricated InP NWs and InGaAs NWs when excited by two different linearly polarized femtosecond laser pulse. ....64

## CHAPTER 1

### INTRODUCTION

#### 1.1. Overview of the Thesis

This thesis starts with an overview of terahertz technologies in Chapter 1. The chapter is divided into three subsections. The first of these shows a detailed outline. The second subsection introduces a brief review of the terahertz related technology. The chapter ends with some the unique properties of terahertz frequency radiation as well as some of pros and cons that will be exploited in the applications.

Chapter 2 provides detailed methodological information of THz technology which have been used in this thesis. The chapter begins with well-known techniques to investigate the terahertz waves. It also introduces brief concepts of the devices that generate and detect the terahertz frequency radiation. The second subsection defines the terahertz time-domain spectroscopy and introduces the entire system – the main equipment what I have been used. The third subsection covers system configurations and optical alignment procedures. It first describes the process of getting the stable laser pulse (mode-locking) and the project that had been prepared for automatic monitoring and controlling. Later it introduces the transformation of the measurement system and alignment know-hows. Chapter 2 ends with a review of data processing including data quality improvement and terahertz imaging capabilities. The third chapter covers flexible absorbers measured by using reflection mode of terahertz time-domain spectroscopy.

This chapter starts with background on flexible metamaterial devices and the inspiration for the work. Then the device simulation, fabrication, and measurement are described in detail. The chapter ends with the comparison of simulation and measurement results as well as a conclusion.

Chapter 4 covers an experiment on bio cells using the transmission mode of terahertz time-domain spectroscopy. This chapter first introduces the brief review over the biomedical application of THz wave and then focuses on the main issue – distinguishing the normal and cancerous human breast cell lines. The second subsection explains the culturing process of the cell, and the third subsection describes the measurement procedures. This chapter ends with the measurement result and conclusion.

Chapter 5 introduces an alternative way of terahertz emission rather than the photoconductive antenna used in the terahertz time-domain spectroscopy; the surface emission of terahertz from nanowires. Likewise the previous chapters, this chapter starts with an explanation regarding the background of the surface emission and principles in the first subsection. In the second section, the modified measurement setup and procedure for the surface emission are introduced. The third subsection explaining the process of fabricating the nanowires using E-beam lithography is also added. This chapter finally ends with the analysis of the result especially on the difference between various combinations of nanowires.

The thesis concludes with Chapter 6 which provides a summary of the findings of the flexible absorber, human breast cell lines and nanowire's terahertz emission projects. This chapter ends with a discussion of possible future work for these projects.

## 1.2. THz Technology Review

The range of frequencies between 0.1 and 10 THz, which lies in the overlapping region of the electromagnetic spectrum between the microwaves and the infrared, and corresponding to wavelengths from 30  $\mu\text{m}$  to 3 mm and photon energies from 0.4 meV to 40 meV, was often referred to as the terahertz gap as shown in the Figure 1.1.

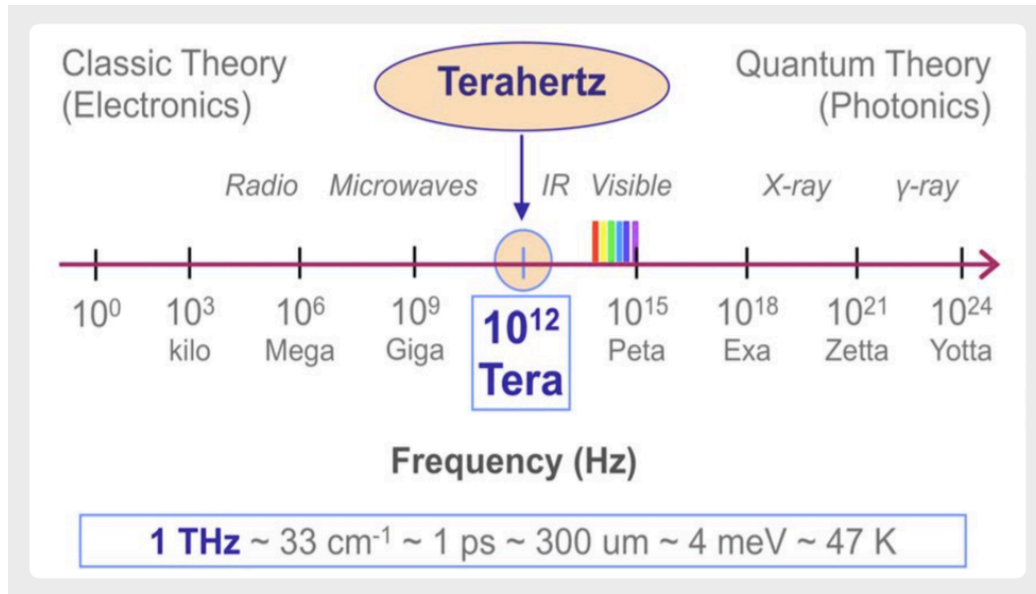


Figure 1.1 The Terahertz band in the electromagnetic spectrum [1]

That was because the wavelength in that region of the spectrum was not utilized until recently unlike most of the other waves in the electromagnetic spectrum. Although the physical functions and properties of THz waves are represented by the Maxwell equations, they are much more complicated than the other electromagnetic waves near to them such as microwave frequency or infrared. For example, the transformation from electric changes into electromagnetic radiation has not used to be effectively achieved through the utilization of semiconductor devices until recently. [2, 3] Generally, exploration on electromagnetic waves was partitioned into two distinct fields: the photonics (or optics) and the electronics as shown in Table 1.1.

	<b>Electronics</b>	<b>Photonics (Optics)</b>
<b>Main agent</b>	Electrons	Photons
<b>Name of waves</b>	Electromagnetic waves	Optical waves
<b>Principle</b>	Maxwell equations	Schrodinger equations
<b>Emission</b>	Classical movement	Quantum transition
<b>Measurement</b>	Electric field	Intensity
<b>Tools</b>	Circuit, Antenna, Waveguide	Lens, Mirror, Fiber
<b>Approximation</b>	Uniform field	Uniform medium

Table 1.1 Comparison of Electronics and Photonics (optics) [1]

That division between Electronics and Photonics almost exactly happens around the THz band, therefore it is called the THz gap. The interesting thing is, in one aspect, THz waves do not simply belong to either of them. For example, electromagnetic waves are typically produced from the floating movement of carriers (electrons). However, most of conventional RF sources cannot produce high-frequency radiation over a few hundred GHz since the movement of the carrier cannot take the pace of THz oscillation. Furthermore in a waveguide, both the metallic waveguides for microwaves and dielectric waveguides or optical fibers for photonics suffer from high loss for THz waves. Despite these difficulties, in another point of view, the THz band is a zone of union between the electronics field and the photonics field. Even though both fields contrast with the theoretical system and technical methodologies as mentioned in Table 1.1, ironically, it makes the THz band a fruitful area for intriguing hybrid systems. Both the electromagnetics and optics fields are worthy of a multibillion-dollar industry. Understandably, the scientific and methodological mixture between the two fields will act as an evolution of their individual industries.

Despite these great possibilities, THz investigations stayed ambiguous because of difficulties of experimental sensitivity, limited device fabrication capabilities, and problematic generation and detection equipment [4]. These restrictions have continued to give researchers much trouble approaching THz technology from both electronic and optical techniques. Figure 1.2 shows the development trend of respective frequency bands in the electromagnetic spectrum. The left side of the figure displays the tendency of utilizing bands from lower to higher frequencies in the electronics industry as the time flows up to recent. On the other hand, the photonics industry has a tendency of utilizing bands from higher to a lower frequency to cover the Far Infrared band. Those industries meet at the THz band, in which systems and applications are being researched enthusiastically nowadays. Lack of maturity and undefined applications opens a big possibility of a future business opportunity to commercialize the design, fabrication, and systems conducting in the THz band that could enlarge the new market and application needs.

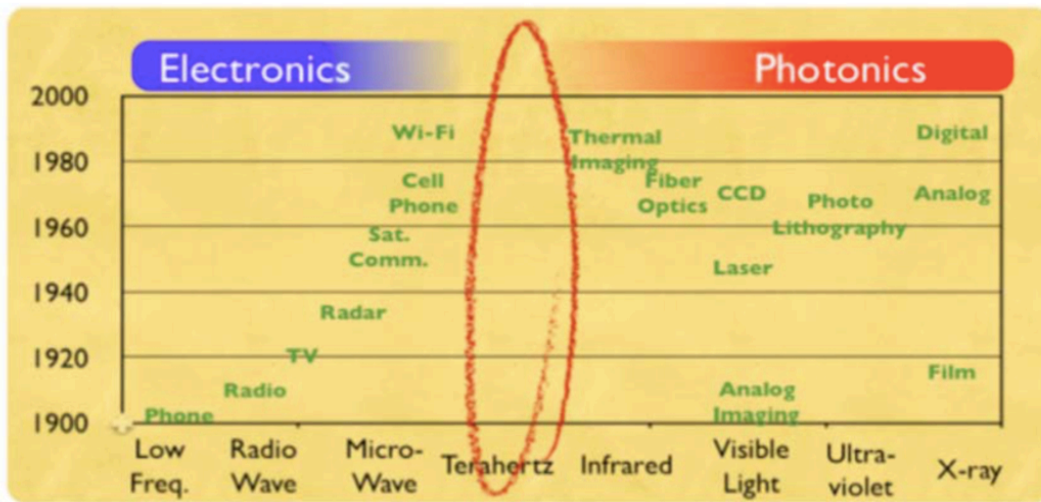


Figure 1.2 Electronics and Photonics industrial convergence [5]

### 1.3. Characteristics, Pros and Cons, and applications of THz waves

There are several vital features and advantages in THz region of radiation rather than other frequencies, which can be utilized for next-generation technologies over various researches, industrial and commercial fields. First of all, THz waves are non-ionizing due to the low photon energy level (0.4 – 40meV), which means the waves are harmless for living tissues compared to X-rays. Also, it can penetrate many non-conductive materials such as clothes, papers, ceramics and plastics while permitting the spectroscopic response of both materials and objects beyond [6-8]. Concretely, “in the same way that visible light can create a photograph, radio waves can transmit sound, and X-rays can see shapes within the human body, terahertz waves (also called as T-rays) can create pictures and transmit information.” [1].

Another essential characteristic is the fact that the rotational and vibrational modes of various molecules, especially organic compounds, scattered around the Terahertz region, which is known as fingerprint effect. This lets THz spectroscopy as a unique characterization technique for sensing organic compositions since even the marginal structural transition can be clearly observed in the changes of THz absorption spectra [9].

THz spectroscopy is also practical in investigating the frequency dependent electrical and optical parameters of materials and devices. Examining the response such as absorption, transmission, and reflection of the THz radiation can provide useful information such as the complex index of refraction, complex conductivity, permittivity, and carrier lifetime [10-14].

Faster communications at a higher frequency than the microwave band is another area of an intensive minefield. As wireless communication technology improves, both the speed of data flow and the overall amount of transmittable information have dramatically increased. Currently, several tens of gigahertz of frequency in microwave band range is the most dominant for fast

wireless communications. Understandably, next progress will be focused on the THz region. It is known that the THz wireless communication promises faster speed by a factor of thousands.

However, THz frequency band also has a few critical disadvantages. Mostly, utilizing the THz requires coherent sources that also require subsidiary equipment, which is currently expensive. Furthermore, THz waves have a limitation in the use of long distances in the atmosphere because water vapors and other gasses absorb THz waves. Because of these issues, utilizing the THz communication is limited to line of sight distance. [15] Finally, there are very few natural sources that can be efficiently utilized to exploit terahertz frequencies band. As a result, it is still difficult to work with THz outside of research facilities. Metamaterials, materials engineered to have properties that have not yet been found in nature, promise new abilities to manipulate radiation at these frequencies.

## CHAPTER 2

### METHODOLOGY

#### 2.1. Techniques for investigation of THz wave

Until the late 1960s, the Globar lamp that used to emit radiation in the far infrared region as a black body THz source, was the only way to generate radiation generation at terahertz frequencies. Finally in the late 1980's, as a significant breakthrough in the THz research, the photoconductive techniques, and optical rectification methods were successfully implemented in the THz region. Those two are the most common research techniques until today. [16-23] Boundless advancements have been achieved through the exchange of antenna devices and implementation of different electro-optic or semiconductor materials. [24-33]

Currently, there are two major technological methodologies in the THz band: the continuous wave (CW) system and the pulsed wave (time-domain system) system. Just like the name of the system, the emission mode and operating frequency discriminates these two methodologies. CW systems use continuous wave for emission and operate at a single frequency or sometimes modulated up to GHz frequencies. As a result, CW systems can only be utilized in narrowband, so it has a limitation in terms of bandwidth, but at the same time, high spectral resolution up to 100MHz also can be obtained. On the other hand, pulsed, so non-continuous systems are usually based on a few picoseconds electromagnetic transient for the generation and detection. The good thing is, unlike the CW systems, the short pulses made up of many

frequencies, which can be converted by using the Fast Fourier Transform provides broadband frequencies that can be utilized. [5]

Currently, although the decisions for selecting system thoroughly depends on the individual research purpose, the THz pulsed method has been the most popular technique in THz research area. Here in this work, especially, in addition to the photoconductive emitters and optical rectification method, surface emitters are to be introduced since it will be discussed in Chapter 5.

Surface field (emission) effect and Photo-Dember effect are the two critical concepts to understand the surface emitters. When an ultra-short optical pulse illuminates a surface of the semiconductor, and when its energy corresponds to the wavelength is above the energy band-gap of the material, the semiconductor generates mobile carriers (electrons or holes). Normally, most of the carriers are generated near to the illuminated surface within 1 micron. THz transients arise either due to the charge separation by the built-in electrical field at the semiconductor surface (Surface field effect) [34] or due to the difference in diffusion coefficients of the electrons and hole (photo-Dember effect) [35]. One of these two mechanisms is more dominant and decides the characteristics depending on the properties such as electron or hole mobility and bandgap energy of the semiconductor material. For example, InAs is a semiconductor material that shows photo-Dember effect with strong high-mobility.

The optical rectification method is perhaps more widespread than the surface emitters and it can generate broadband radiation with a range of 0.1 THz to 40 THz. [36] It was first introduced in 1962 [37] and successfully used in 1989. [38] Optical rectification is a rectifying process of the polarization of a high-intensity pulse by using the nonlinear response of a crystal structure. During the process, total internal reflection (TIR) will keep the generated terahertz

beam inside of the crystal until it meets proper lens, normally sapphire or silicon, which admits the terahertz beam to be emitted into the free space.

The photoconductive emission method had been developed during the same period when the optical rectification method arose. [39-41] It utilizes a device called the photoconductive antenna (or PCA) that emits broadband terahertz frequency radiation. When the photon energy of the laser pulse that illuminates the crystal material is higher than the band gap of material used for the photoconductive antenna, it absorbs the energy and excites the photocarriers along the material. THz emission is generated by the acceleration and subsequent recombination of these photo-carriers. The voltage bias applied and transmitted to the antenna creates a strong electric field and helps to accelerate the photocarriers so that the antenna can generate the intensive pulse. There are a lot of different types of PCA with various materials and shapes, but most of them typically have thin or parallel metal strips facing each other across the crystal surface.

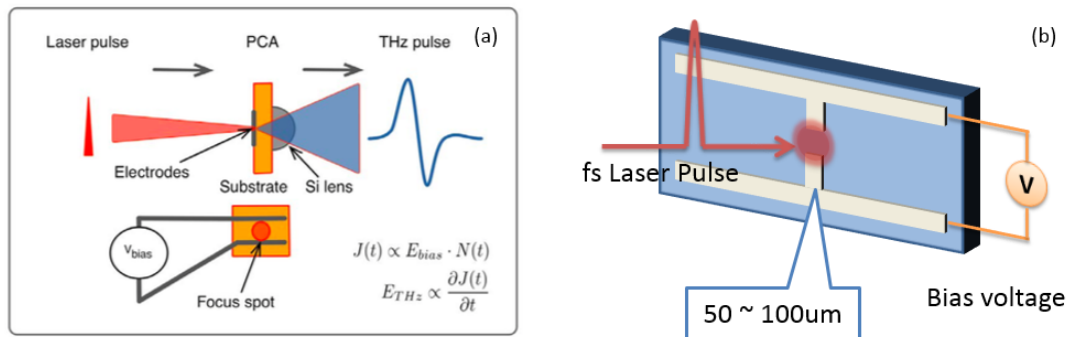


Figure 2.1 Diagram of (a) typical PCA generation mechanism [5] and (b) principle of THz emission from PCA

The PCA also can be an efficient method for detection in typical pump-probe systems. Just like when it is used to emit THz waves, the antenna must be photo-excited by the laser pulse with high enough energy to allow the inter-band carrier transitions. The surface current in the antenna can be measured when the THz pulse hits the antenna at the same time as the probe laser

pulse, because it will be proportional to the electric field of the incident terahertz pulse. PCA as a detector has several specific advantages. Since the incoherent radiation is filtered when it detects the signal, and since the sampling time per data point is very narrow, it shows high sensitivity regarding signal-to-noise ratio. Furthermore, PCA antennas are mostly as small as conventional microchips and so portable. However, just like the two sides of the same coin, it yields tremendous difficulty when the user aligns the optics because the effective area of sensitivity is tiny like a few tens to hundred microns as shown in Figure 2.1(b). PCAs also have a tendency to provide narrow bandwidth after Fast Fourier Transform (FFT) than the other common method of detection; the electro-optic sampling.

Electro-optic sampling utilizes Pockel’s effect (first described in 1906 by Friedrich Pockels), which represents the phenomenon such that the modulation of birefringence occurred in an electro-optical crystal when an electric field applied to the crystal. In the typical THz pump-probe system, when the two beams -THz wave and the pulsed laser as a probe beam- collinearly propagated into the electro-optical crystal, the electric field of THz pulse changes birefringence (refractive indices) of probe beam, which induces phase modulation of the laser pulse. This differently polarized beam is separated into two components by Wollaston prism and is finally measured by the two balanced photodiodes as shown in Figure 2.2.

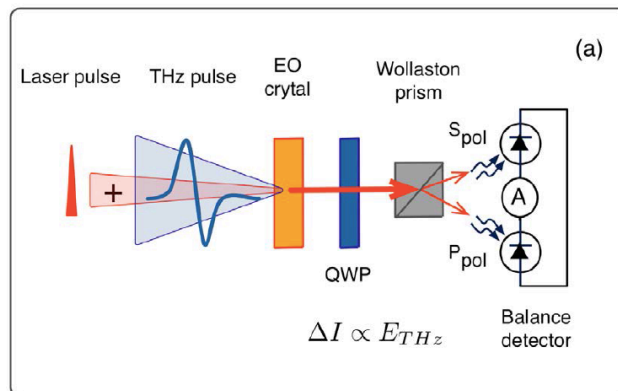


Figure 2.2 Scheme of Electro-Optical Sampling [5].

One noticeable advantage of this method is a broad bandwidth from 0.1 THz to 100 THz depending on multiple crystal materials. [42] However, worse than the PCA detection method, alignment is extremely difficult and time consuming.

## 2.2. THz-Time Domain Spectroscopy

### 2.2.1. System Introduction

The Terahertz time-domain spectroscopy is a spectroscopic method for THz domain frequency investigation. It uses ultra-short pulses of terahertz radiation that lasts only a few picoseconds to probe the properties of a material. Although there are several methods to investigate THz region in the electromagnetic spectrum, THz-TDS is widely being used since it gives the material's characteristics on both the amplitude and the phase.

To have the ultrafast femtosecond pulsed laser in our lab, we are using equipment from the *Coherent* as described in Figure 2.3. The *Verdi Single FAP (Fiber Array Packaged) laser system* provides single-frequency Nd: YVO4 green (532nm) laser, and the *MIRA-900B* converts the green laser to the mode-locked Ti: Sapphire ultrafast red laser that provides 120fs pulses with a repetition rate of 76MHz. The wavelength is tunable from 710 to 910nm but is set at 780nm for our TDS system. That wavelength is specifically related to the band gap of the low-temperature grown GaAs (LT-GaAs) photoconductive antenna (PCA) which emits THz electromagnetic field inside of the TDS system.

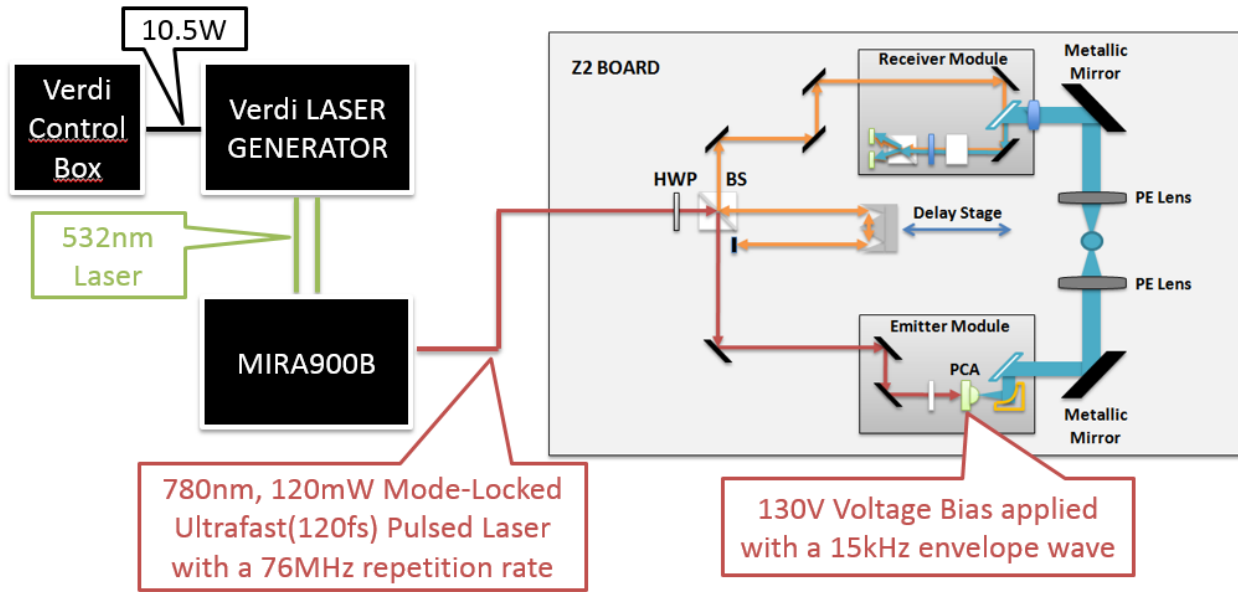


Figure 2.3 Diagram of Laser Pulse Generation and the THz-TDS system

### 2.2.2. TDS System

The TDS is a THz-TDS system with a photoconductive type emitter and an Electro-Optic Sampling type detector. The principle of the emission and detection of THz is as shown in Figure 2.4. The system is composed of multiple optical mirrors, a beam splitter, delay stage and THz emitter and receiver modules as illustrated in Figure 2.1. Each module is connected to the external lock-in amplifier (SR830) to modulate the frequency of the emitting pulse and to process the detected electric field at that frequency as a digitalized signal. A control computer is connected to the TDS system by using the serial port and cables, and the ‘LabVIEW’ program is designed to operate the lock-in amplifier and the delay stage.

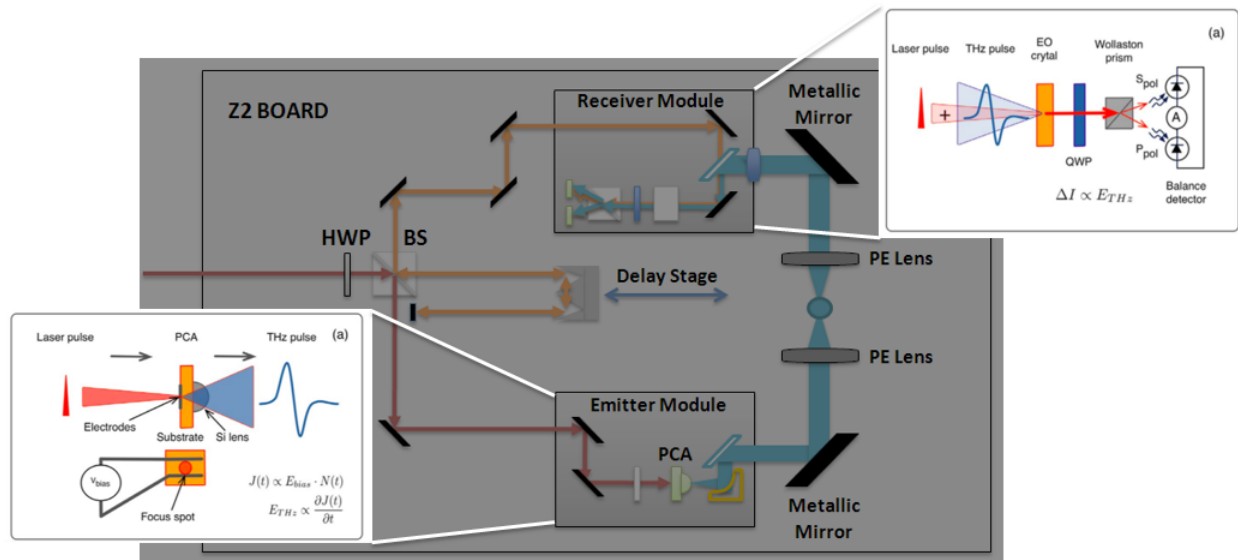


Figure 2.4 The principle of the emission and detection of THz in TDS [5]

In this system, the pulsed input laser beam is divided by a beam splitter into two beams, the pump beam and the probe beam. The pump beam excites the photocarriers in the dipole type band gap of LT-GaAs PCA so that it can emit THz. When the laser pulse excites the photons in the PCA, we apply a high voltage bias of 130V with 15 kHz of modulation frequency. This emitted THz wave travels through the metallic mirrors and lenses equipped on the optical board and finally reaches the detector in the end. If the emitted pulse were not modulated by that 15kHz frequency, the detector would not be able to identify the transmitted THz pulse because there always exists background noise. The probe beam is aligned to come to the detector in advance and interacts with the electric field of incoming THz pulse. This interaction is controlled by the delay stage, which changes the timing of gating laser pulse, resulting that the user can scan the amplitude of the electric field of THz pulse as a function of time.

## 2.3. System Configuration and Optics Alignment

### 2.3.1. Generating Stable Laser Pulse (Mode-Locking)

To perform an experiment, obtaining a stable laser pulse has been a significant issue because the system conditions such as input/output power, knob position over the system were sensitive and have slightly been changed day by day. Converting a continuous laser to pulsed laser is achieved simply by pressing a button name 'GALVO Switch' but maintaining that condition has accompanied adjusting knobs on top of the cover box of *MIRA900B* as shown in the Figure 2.5.

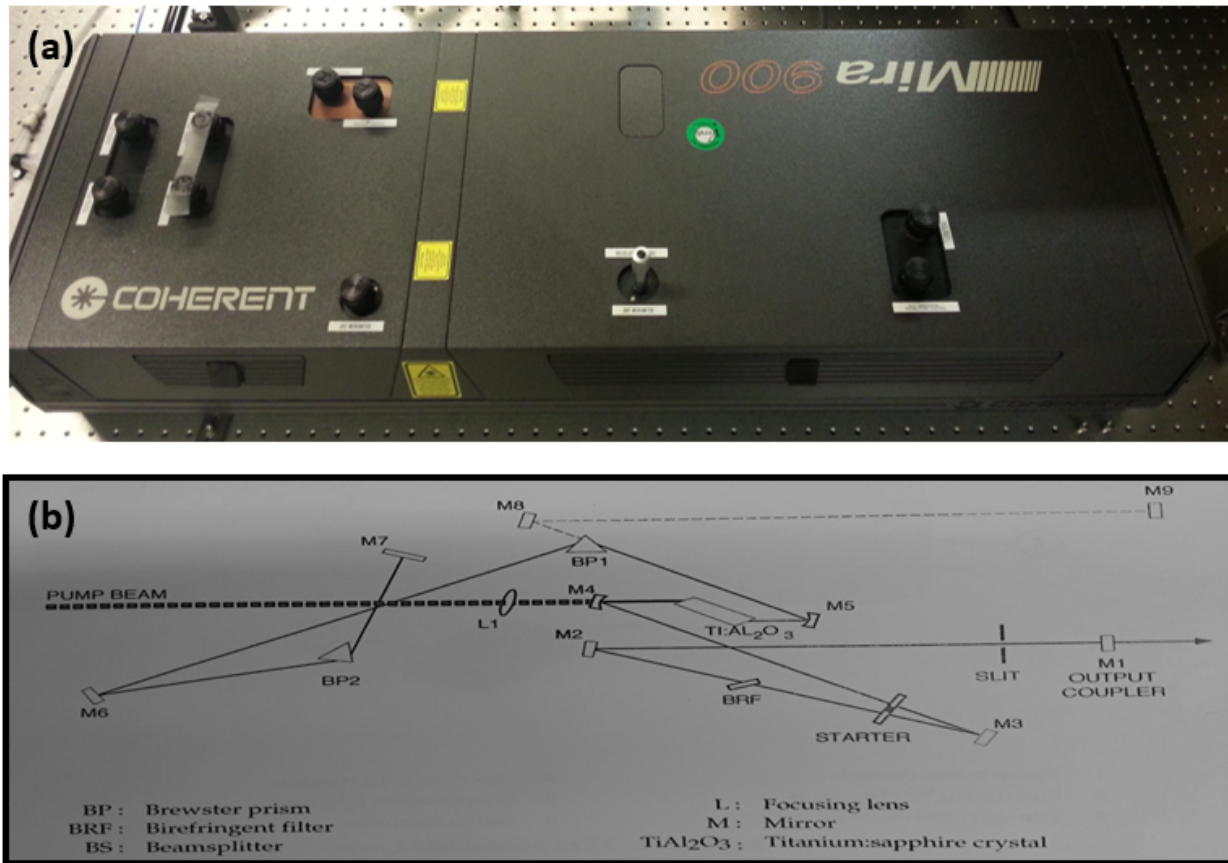


Figure 2.5 (a) Picture of *MIRA900B* and (b) optical schematic diagram inside [43]

When the pulsed laser emitted, it is so called 'mode-locked.' Once the mode lock is lost, in other word the laser returned to the continuous wave, normally it is recoverable by adjusting the 'slit width' knob and M7 knob as shown in Figure 2.5 very slightly. However, when the user loses mode-lock completely, it is hard to recover to the previous condition unless open up the cover of *MIRA900B* to see the beam path, actual mirrors and components. Since it takes significant time to realign all the mirrors and the components, and it is not recommended to have a specialist from the seller company just for that, we only had to adjust the knobs to get back the stable mode-lock by ourselves. An official procedure is written in the manual; it cannot be used until opening the cover box of *MIRA 900B* since there is a prerequisite procedure to follow the procedures. Getting stable mode lock is considerably important because it has a tendency to lose the mode-locked condition when the output pulse is weak. At times, it is unable to get a stable mode-lock even if the user could get it before letting the beam goes into the TDS system. It happens when the pulsed IR laser beam is reflected back by metallic system components such as reflective semiconductor surface and metallic mirror. Those force the laser get back to the same path to the *MIRA 900B* light source and interfere with mode-locking. In that case, the user has to find out the mirror that reflects the beam back and re-align those. Without the pulsed laser, the system cannot properly generate and detect the THz wave, which resulting inoperable status.

### 2.3.2. Software Development for Verdi Control and Mode-Lock

Sometimes, THz spectroscopy has to be run for many hours or a day. There have been several cases in which the mode lock was lost, and the user was not aware of the condition and lost a significant amount of time. Since operator cannot just stand by the equipment until the measurement finishes and losing mode-lock happens irregularly and is unpredictable, this

motivated us to make a program that automatically controls the laser power and sends a notice to the designated user when the experimental condition changes. Thus, we decided to create a program that can monitor the mode lock status of a laser, and notify the user and turn off the laser in case the mode lock is lost. This program can help the user to be notified in those cases to restart THz spectroscopy or imaging measurement as soon as possible.

Figure 2.6 shows a schematic representation of the set-up to be controlled and its algorithm. Controller block controls the Nd: YVO<sub>4</sub> green laser that has 532nm wavelength through controlling the current of a semiconductor laser which pumps Nd: YVO<sub>4</sub> laser. Nd: YVO<sub>4</sub> laser in turn pumps TI: Sapphire laser and TI: Sapphire laser pumps a THz spectroscopy set-up.

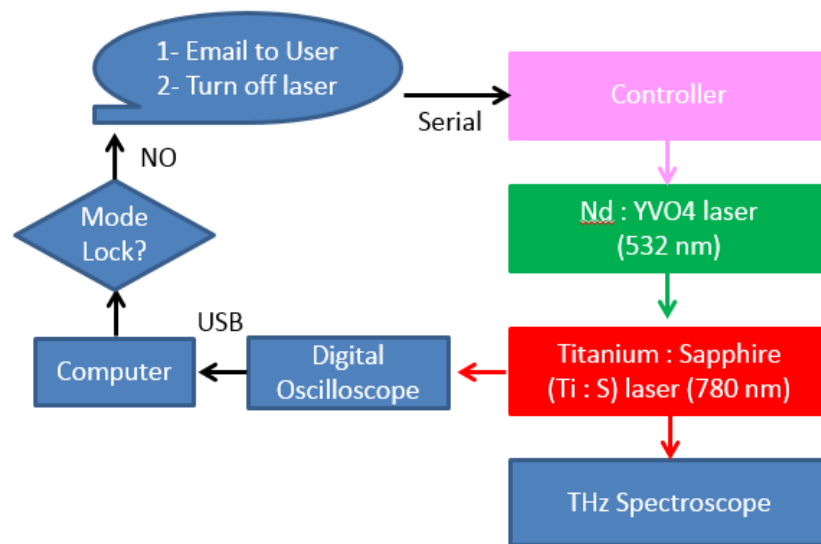


Figure 2.6. Schematic representation of the set up to be monitored.

TI: Sapphire output is detected by a photodiode and a digital oscilloscope captures the created voltage. The main part of this program is to communicate with oscilloscope through a USB port and after getting the data and monitoring the signal, the program is supposed to send email to the user and communicate with controller through a serial port to turn off the laser Nd: YVO<sub>4</sub>.

Figure 2.7 demonstrates a picture of the set-up and the mode-locked and non-mode-locked signal on the oscilloscope.

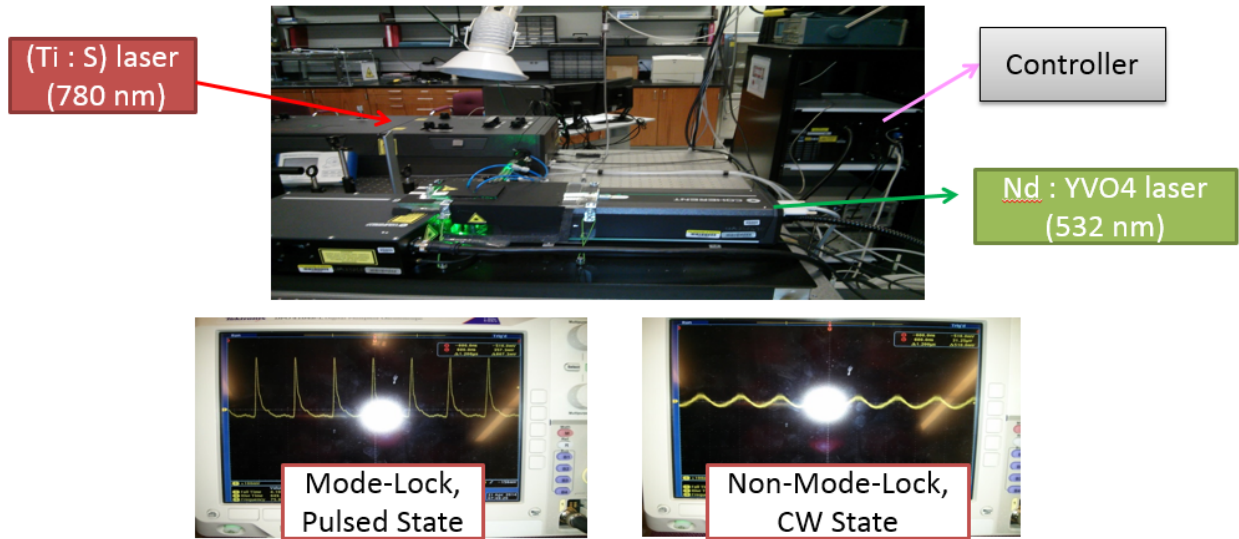


Figure 2.7 Picture of set-up, mode-locked and non-mode-locked signals displayed by digital oscilloscope.

Figure 2.8 illustrates front panel of the VI which is called ‘Main.’ It has an XY graph and two parts embedded in two tabs namely ‘User’ and ‘Advanced’. ‘User’ tab which is more user-friendly includes the addresses for oscilloscope and controller (Verdi), laser channel menu ring to choose the channel which laser is connected to, recipient name, email address, and cc, and indicator to display the status of mode lock. It also has additional controls and indicators like the front panel of an oscilloscope for turning on/off channels, inverting them and running or stopping the oscilloscope. Advanced tab includes advanced parameters to get the data from oscilloscope such as waiting time which determines waiting time between reading and writing the data, start/stop points of data to be obtained, format of the data to be communicated which could be ASCII or Binary, and indicators such as ‘Raw Voltage’, ‘Real Voltage’, ‘ASCII/Binary String’, ‘header’ which determines whether the returned queries from oscilloscope include

header or not, and ‘Return count out’ to show the number returned bytes from oscilloscope. Figure 2.8(a) and (b) show two graphs of mode lock state with two different stop points respectively 1000 and 300.

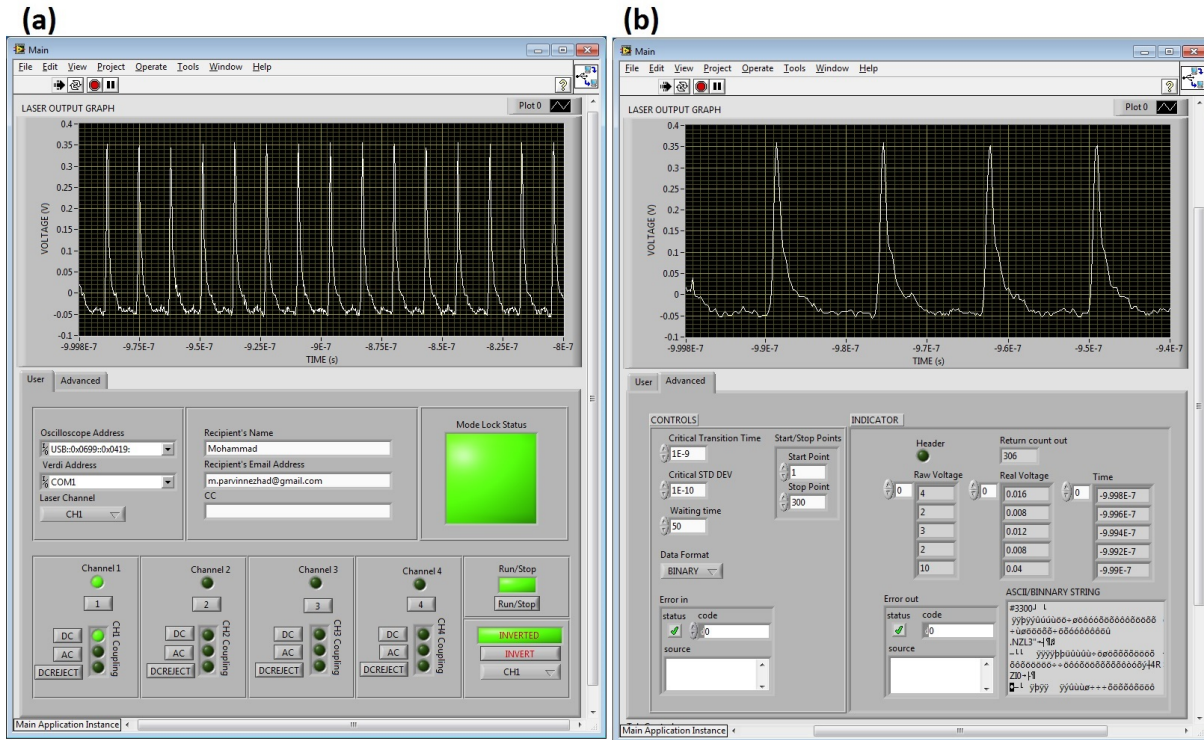


Figure 2.8 The front panel of the main VI (a) with stop point is equal to 1000 and user tab view, (b) with stop point is equal to 300 and advanced tab view.

Block diagram of this VI is represented in Figure 2.9. It includes two sequences. The first one is default settings for the VI, which are applied by using different SubVIs. The second part includes an event structure embedded in a while structure. This sequence creates the major part of the program.

In general, we have used 22 events for this program. It includes events for time out, run/stop, invert channel, channels on/off buttons (4 events), channel couplings (12 events), start/stop points, laser channel, and data format. Total number of SubVIs used for creating this VI is 73

such that 'ReadWriteQuery' subVI is the basic SubVI for reading, writing, and query tasks that were used in creating most of the other SubVIs (Figure 2.10).

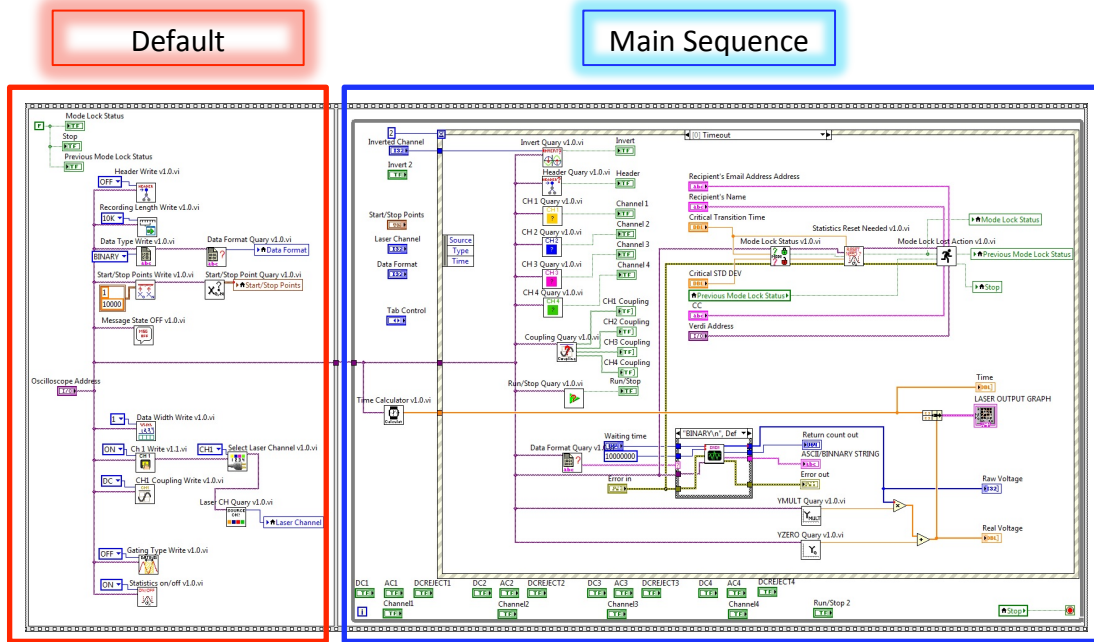


Figure 2.9 Block diagram of main VI including two sequences for default settings and event structure inside a while loop

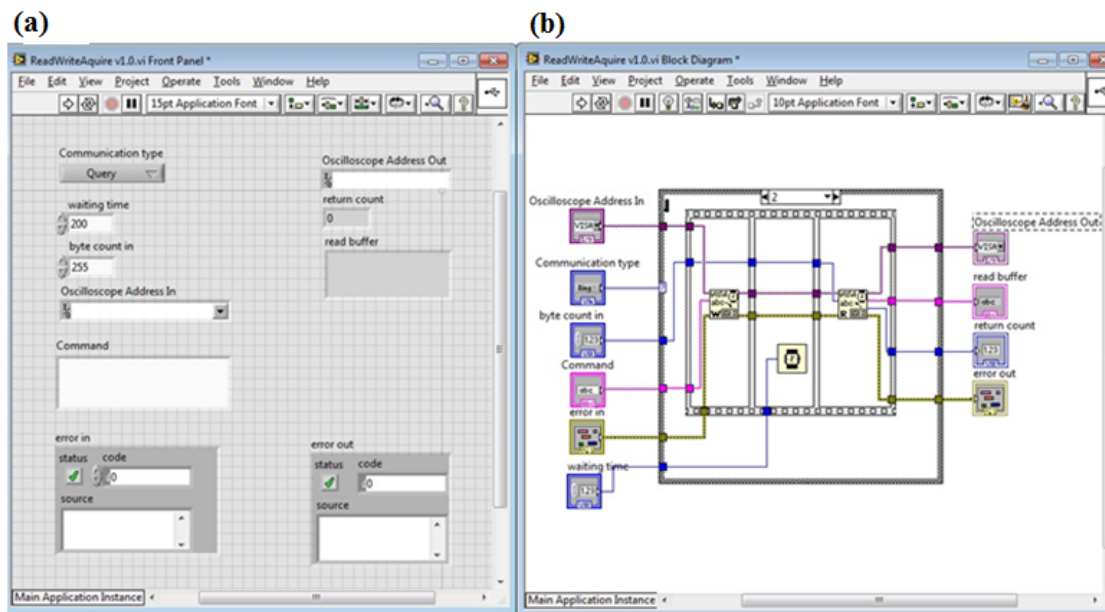


Figure 2.10 The front panel (a) and block diagram (b) of basic 'ReadWriteQuery' SubVI.

The timeout event can be categorized into four parts which include ‘Front Panel Queries’, ‘Data Acquiring’, ‘Real Data and Time Calculator’, and ‘Mode Lock Check and Operation’. This category is demonstrated in Figure 2.11. The ‘Front Panel Queries’ includes status queries for channels on/off modes, oscilloscope run/stop modes, channels inversion mode and AC/DC coupling modes of channels. ‘Data acquiring’ part includes SubVIs for acquiring data in either Binary or ASCII format. The data format has a control button as an event case in the front panel to choose between binary and ASCII types. A SubVI called ‘Data Format Query’ which asks oscilloscope the format of acquired data, is connected to a case structure including two instances of Binary and ASCII with corresponding SubVIs in any case. One of the outputs of these SubVIs is numerical array called ‘Raw Voltage’ which needs to be converted into real voltage values in ‘Real Data and Time Calculator’ category by using  $Y_i = YZERO + (YMULT \cdot DataPoint_i)$  where Y is the real voltage, YZERO and YMULT are queried by using corresponding SubVIs and DataPoint is raw voltage. Accordingly, time which is the horizontal axis can be calculated by  $X_i = XZERO + XINCr \cdot (i - 1)$  where X is time and XZERO and XINCr are queried by using corresponding SubVIs. The block diagram of SubVIs for acquiring binary and ASCII data are shown in Figure 2.12 and 2.13.

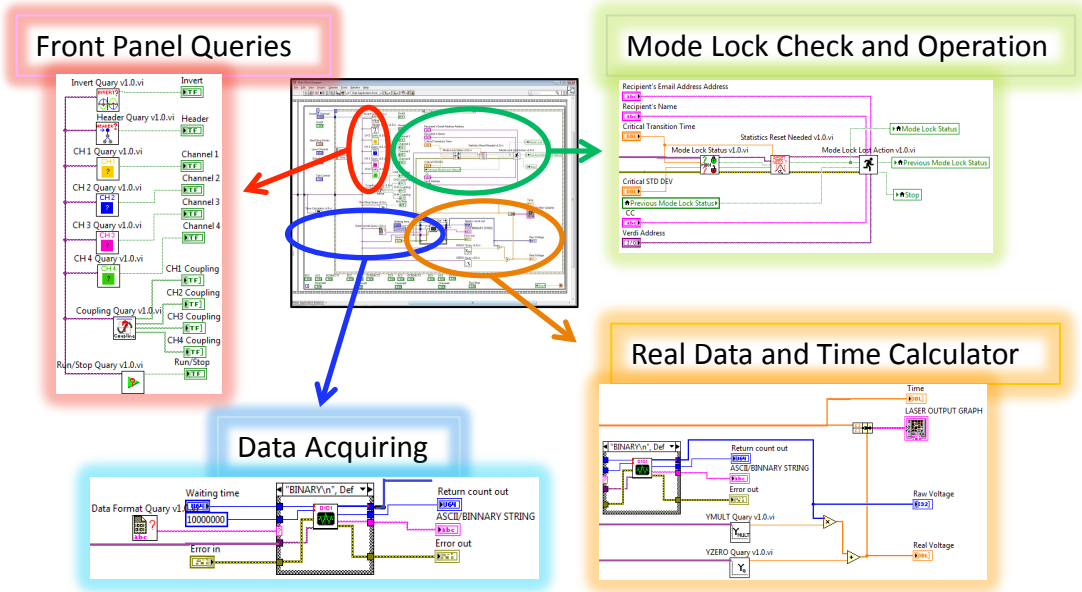


Figure 2.11 illustration of four major parts of timeout event.

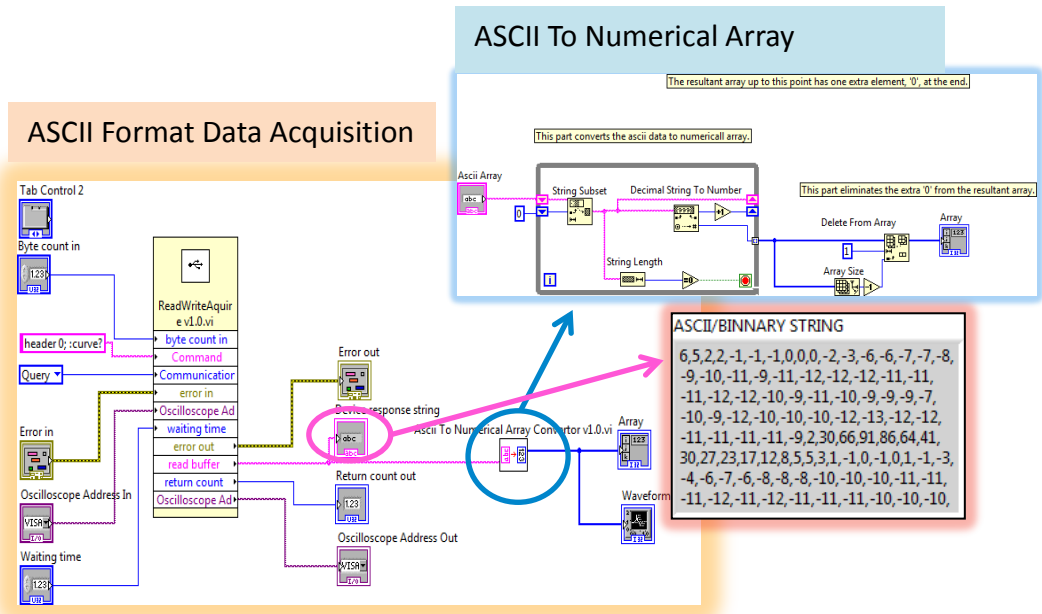


Figure 2.12 Block diagram of 'ASCII Format Data Acquisition' SubVI.

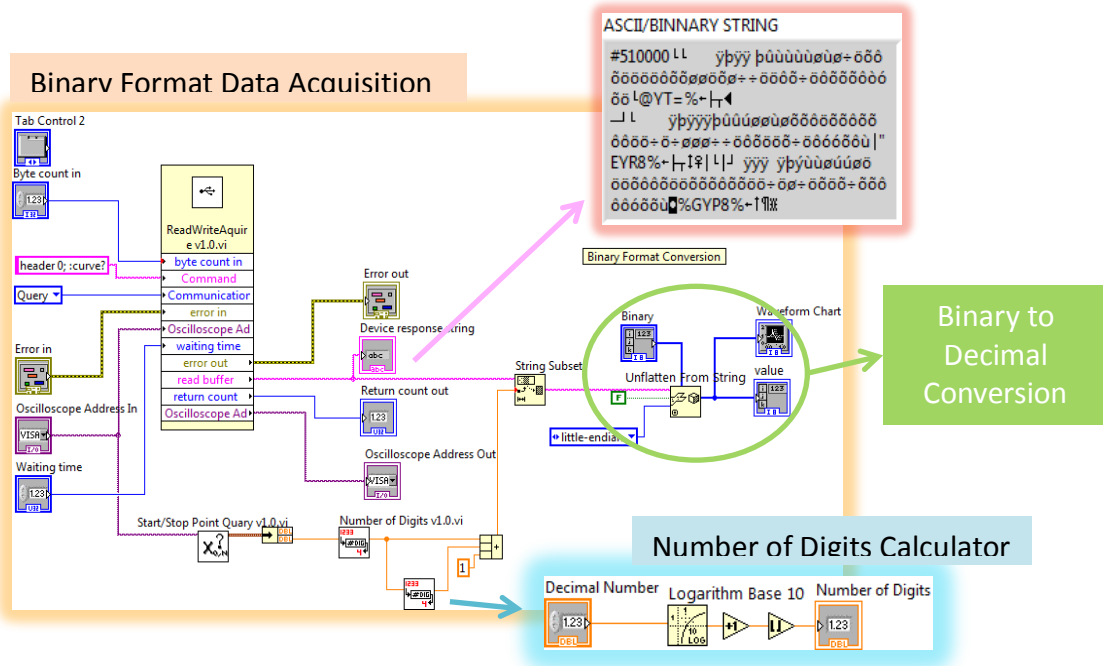


Figure 2.13. Block diagram of 'Binary Format Data Acquisition' SubVI.

The last section of time out is the checking mode lock status of the laser and operating required actions such as emailing to the user and turning the laser off. Figure 2.14 shows this part by a close view. Mode-lock status is a SubVI, which determines the mode lock status by using rising or falling time (transition times whichever is smaller) and the standard deviation of this number. The maximum value and standard deviation for transition time is 1 ns and 100 ps in mode lock case. 'Statistics Reset Needed' SubVI checks whether statistics reset is required or not. When there is no mode lock signal and the mode lock comes back, statistics takes a long time to get lower than a critical value. Resetting Statistics solve this problem and helps standard deviation stabilized quickly. The last SubVI is 'Mode Lock Operation' which sends email, turns off the laser, stop the program, and displays a text message on oscilloscope, in case mode lock status

goes from 1 to 0. Figures 2.15, 16, and 17 show the SubVI of ‘Mode Lock Check and Operation’ category.

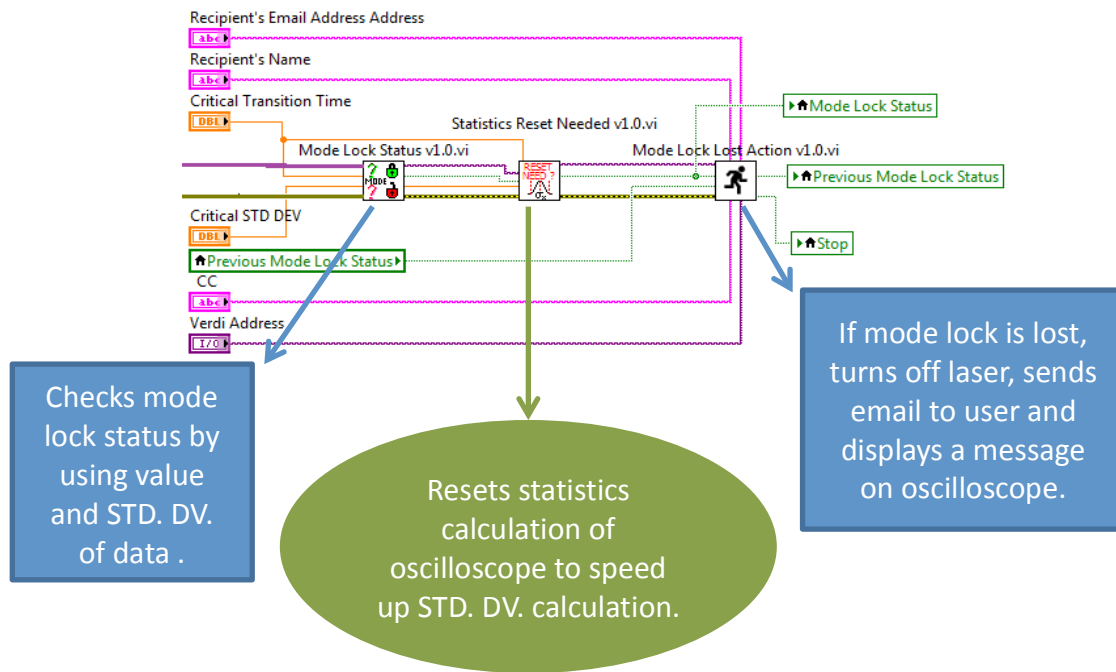


Figure 2.14 Close view of Mode Lock Check and Operation category of timeout.

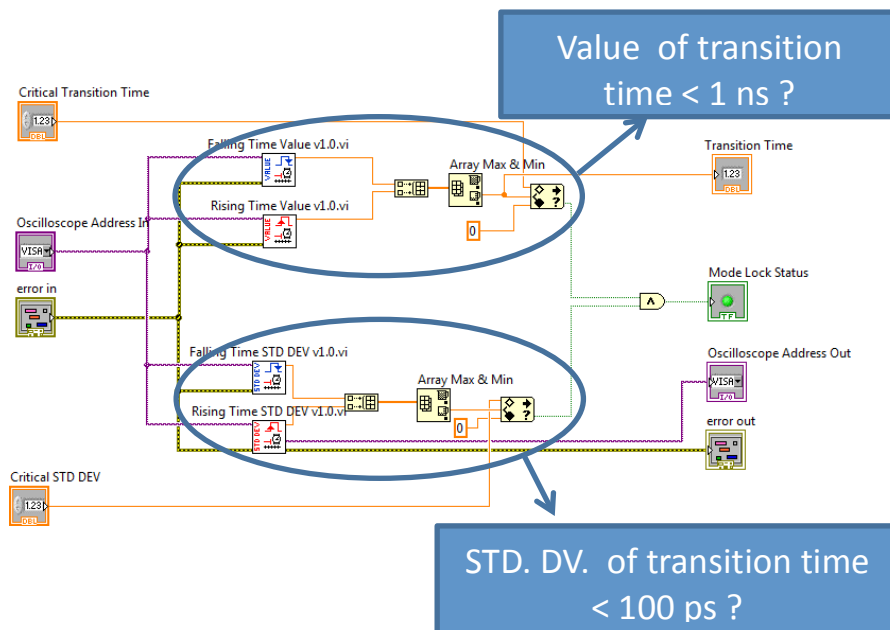


Figure 2.15. Block diagram of ‘Mode Lock Status’ SubVI.

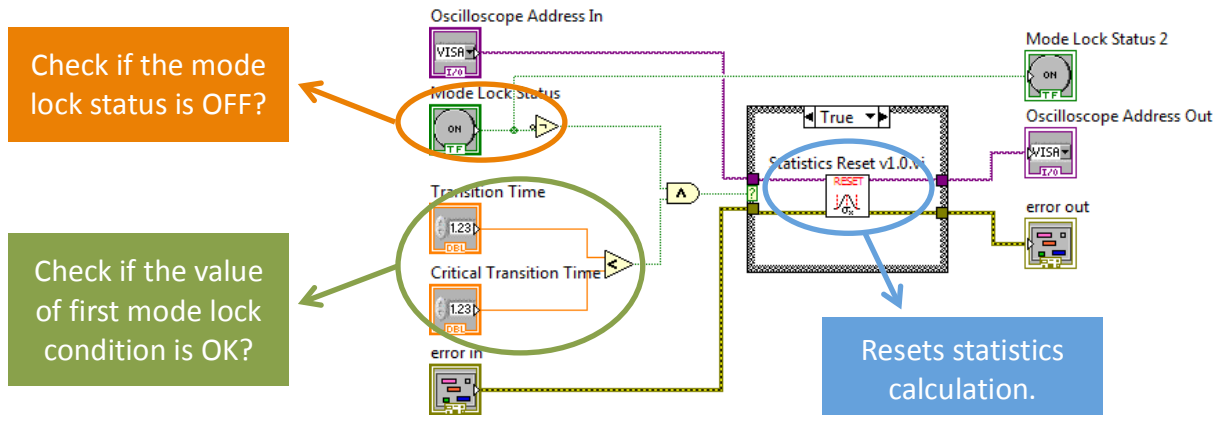


Figure 2.16. Block diagram of 'Statistics Reset Needed' SubVI.

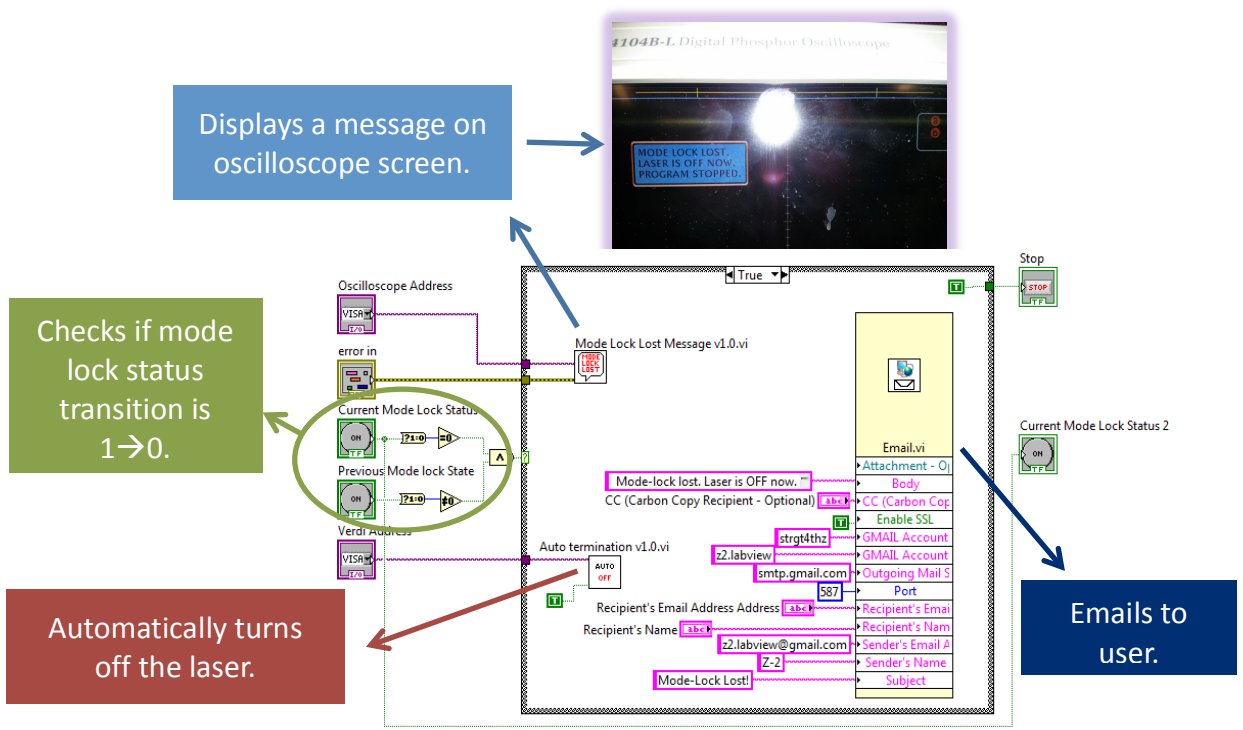


Figure 2.17. Block diagram of 'Mode Lock Lost Action' SubVI.

### 2.3.3. Experimental Mode Transform and Optics Re-alignment

There are two experimental modes for utilizing the TDS: the transmission mode and the reflection mode as shown in the Figure 2.18. For either purpose, the user needs to know where the beam is passing through to put the polyethylene lenses and samples in the appropriate position so that the sample can get a maximum intensity of THz wave. Since the THz wave is invisible, the operator needs kind of reference for the beam alignment, and the alignment laser provide the approximate position information of beam path.

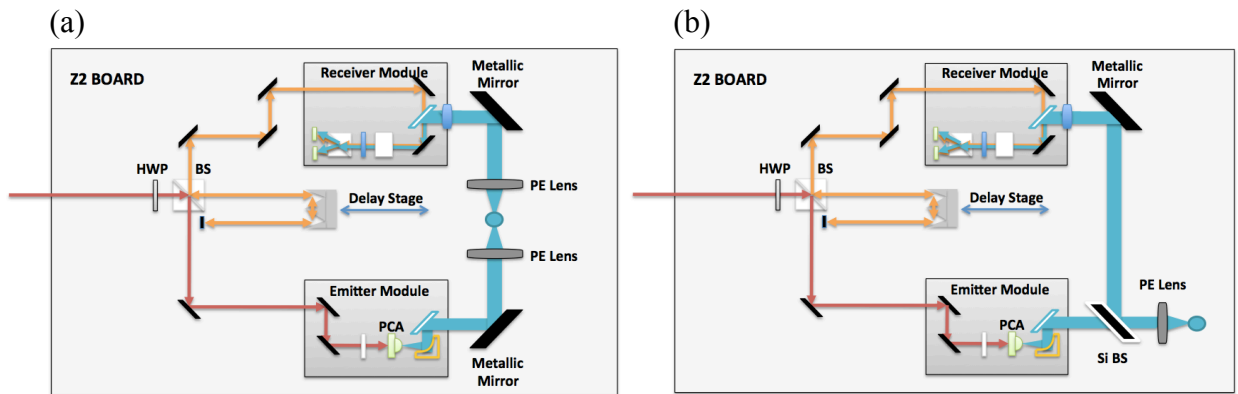


Figure 2.18 Diagram of the (a) transmission mode and (b) reflection mode scheme

The general procedure to make the alignment laser and THz beam collinear in the transmission mode scheme is as follows. First, the user must get the most THz amplitude by scanning a window that has a THz peak. And then the two irises have to be placed between the emitter and detector mirror. Placing them as close as possible to each mirror is recommended. After connecting the oscilloscope and the lock-in amplifier, the user can start using the ‘dithering around max’ function in the LabVIEW program so that the user can observe and control the real-time peak intensity of THz. While the delay stage dithering the peak position as well as leaving the iris fully opened, user can gradually move one of the irises to both horizontal and vertical direction one by one until identifying the estimated location of THz beam. After fixing the irises

at that position, the user can slowly close the irises and again perform the tiny adjustment by watching the real-time signal changes. Gradual closing and axis adjustment will lead the user to have perfect alignment. When it is well aligned, in other words, when the THz beam passes through the tiny hole in the iris, the user can still get reasonable amplitude. Once the location of THz beam is identified, the only thing left is adjusting the inner mirrors for the alignment laser until it can pass through the hole of two irises. While setting up the alignment beam, it is better to make it as straight as possible between the two metallic mirrors of emitter and detector. Using the alignment laser will also help when the user put the Poly Ethylene lenses in the proper position.

Transforming to the reflection mode is simple if the transmission mode is well aligned. First, from the well-aligned condition of the transmission mode, the metallic mirror on the emitter side has to be taken off. After that, it is recommended to place one or two more another irises on the beam path so that it can pass through the irises. Placing another alignment laser after the irises is essentially required. If the laser beam passes exactly through the iris and another laser source, they are collinear each other. Replacing the beam splitter at the position of the metallic mirror on the emitter side is the last step for the reflection mode alignment. The user can utilize the alignment laser for setting the position of the sample holder and a PE lens.

## 2.4. Data Processing

### 2.4.1 THz Waveform Acquisition and Conversion

To analyze and characterize the property of measured data in terms of frequency, the frequency domain data need to be obtained. The Fast Fourier Transform (FFT), an algorithm to compute the discrete Fourier transform (DFT) can be utilized for the frequency domain data

acquisition. Developing the Time-Domain Spectroscopy was a powerful solution to utilize this FFT algorithm.

In our THz-TDS system, the voltage of THz waves detected by photodiodes is directly delivered to the lock-in amplifier. After processing this value into a digital signal, the lock-in amplifier provides this data to the LabVIEW program that was designed to control the system remotely. This program displays the detected voltage value as a function of the corresponding position of the delay stage which represents the relative distance of the probe beam that travels before reaching the detector. Even if the speed of delay stage increases, the voltage waveform is displayed in fixed resolution of distance; 1um by interpolating between the two data points. This x-axis data, the relative position of the delay stage in fixed resolution, can be converted into the fixed time interval, which allows to use FFT. Converting the distance to the time is performed by a calculation of basic equation between the time and distance. Since the resolution of the delay stage recorded by system is fix in 1 micron, and 1 micron of distance in delay stage corresponds to 4 microns in the detector due to the scheme of the reflecting mirrors on delay stage, the time interval for unit distance in micron scale can be calculated as shown in the below.

$$Time\ interval = \frac{4\mu m}{speed\ of\ light} = \frac{4 \times 10^{-6} m}{3 \times 10^8 m/s} = 0.0133 ps \quad (2.1)$$

Therefore, a fast Fourier transform (FFT) is performed based on the time of 0.0133ps with the number of data points defined by window size to generate frequency dependent values of power, amplitude, and phase. The FFT is derived from the equation of discrete Fourier transform as follows.

$$y_k = \sum_{n=0}^{N-1} x_n e^{-i2k\pi \frac{n}{N}} \quad (k = 0, 1, 2, \dots, N - 1) \quad (2.2)$$

Where  $y$  is the transformed frequency dependent data,  $N$  is the number of data points, and  $x$  is the input time domain data. [44] A Typical time-domain waveform obtained by THz-TDS and converted signal by FFT is as shown in Figure 2.19.

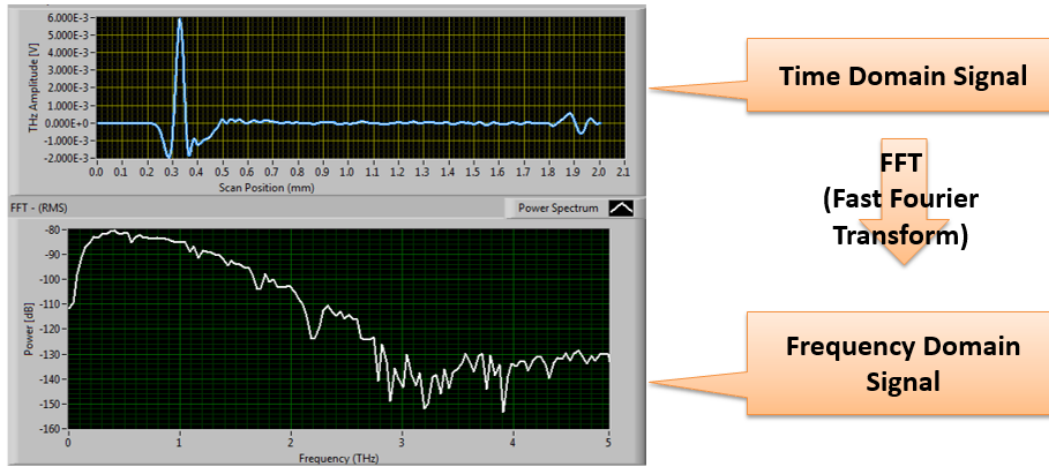


Figure 2.19 Typical time domain THz pulse in the air and its transformation into frequency domain data

#### 2.4.2. Extracting Information and Improving of Signal Quality

Analyzing the frequency domain signal is normally based on identifying the transmission or reflection ratios for a given sample. To do that, an additional measurement for reference must be performed. The scan of reference must target the identical materials or the signal through the air that in the sample scan, except for the sample itself. After that, when the frequency dependent amplitude of the sample is divided by that of the reference, the transmittance or reflectivity depending on the measurement mode can be obtained. This process became easier by using additional LabVIEW program named ‘THz Analyzer’, a home-made program that was written by a previous student in our lab. While processing the data, most of the THz systems displays echo of the original pulse because of the Fabry-Perot reflections or internal reflection from the

optical components such as beam splitters and lenses. If such echoes are processed together in the Fourier Transform, interference happens such that the result shows multiple sinusoidal features known as etalon effect. [5] This makes the analysis troublesome and they conceal real signal features. Thus, removing the echoes from the original time-domain waveform is crucial in the analysis. An example of removing the ‘etalon effect’ is as shown in Figure 2.20. It shows a comparison between the raw data and processed data. It clearly shows the artifacts in (a), and become smoother out after the proper signal processing in (b).

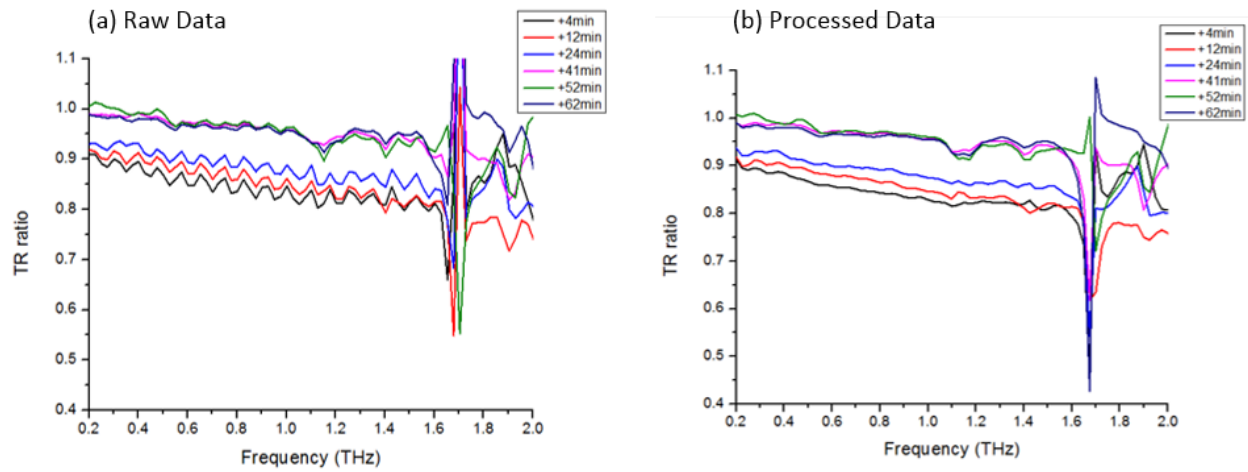


Figure 2.20 Frequency spectrum comparison of (a) row data and (b) processed data after removing the etalon effect from the time-domain waveform

In addition, to fully acquire meaningful information from the frequency domain waveform, improving the resolution of the frequency spectrum is essentially required. Favorably, it can be simply achieved by expanding the size of window in the time domain measurement so that it can have an abundant number of data points. However, due to the limitation of communication speed, increasing the window size necessarily requires additional measurement time. If the speed of the delay stage increases to avoid a loss of time, the data resolution also will be decreased. Furthermore, expanding the window size increases the possibility of having more

echoes or internal reflections. Unfortunately, removing the echoes sometimes necessarily forces to cut the original waveform, which results in losing the number of the data points. Therefore, sometimes we do additional processing after cutting off the echoes to increase the number of data points as a mathematical solution. By taking into account the etalon effect, we can acquire much smoother waveform.

Even though the above procedure can smooth the frequency domain waveform, it cannot eliminate the absorption peaks caused by water vapor in the air. Multiple water absorption lines usually detected in our system are as shown in Table 2.1.

Water Vapor Absorption			
Line Frequencies (in THz)			
1.09	1.72	2.26	2.77
1.16	2.17	2.39	2.97
1.67	2.2	2.64	3.01

Table 2.1 The absorption lines in the THz-TDS spectral range due to atmospheric water vapor. [45]

Within the effective range of frequency spectrum in our system, let say 0.2 to 2THz, which is dominant spectrum region we use in our measurement, two distinct absorption lines exist around 1.1THz and 1.7THz. The ordinary process used to reduce these lines is purging the system in the enclosure box. To achieve this, acrylic enclosure that is connected with dry air and nitrogen (N<sub>2</sub>) gas valves was assembled for the system. Once the dry air or nitrogen (N<sub>2</sub>) starts purging the system from the top of enclosure box, it forces air with the water vapor to go out. It usually takes 15 minutes to reduce the effective humidity using this method in our lab. The effectiveness of the purging can be compared as shown in Figure 2.21. It shows the transmitted power spectra from 0 to 2 THz before and after purging.

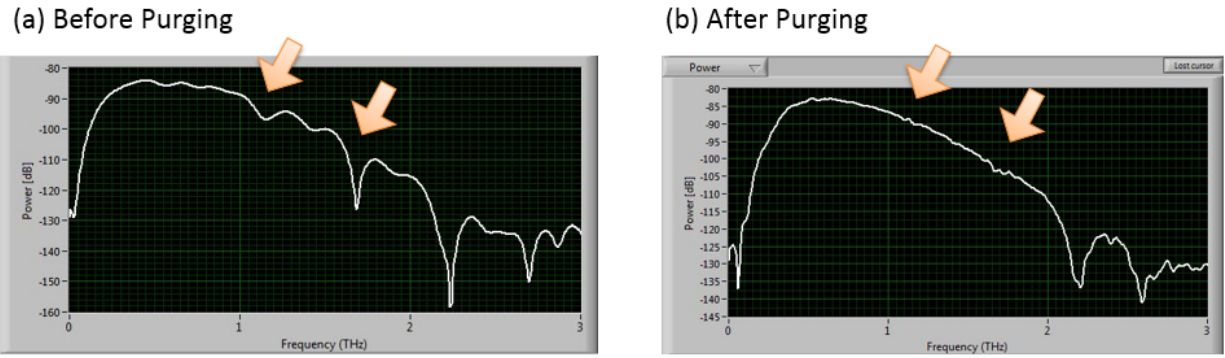


Figure 2.21 Power spectra comparison between (a) before and (b) after purging with N<sub>2</sub>

## 2.5. THz Imaging

Terahertz spectroscopic imaging can be executed with the transmission mode by handling the motion controlled stage as shown in Figure 2.22. This can be achieved by spectroscopic scanning of the sample in the perpendicular plane to the terahertz beam path. A set of pixels composed of each scan builds up a spectroscopic image by mapping the sample position coordinates, in terms of x-axis and z-axis. While constructing an image, the target sample moves along these axes by 3-axis motion controller with designated range and step size. For all three axes, this motion controller provides a maximum translation range of 20mm with a minimum repeatable step of 8 $\mu$ m. [46]

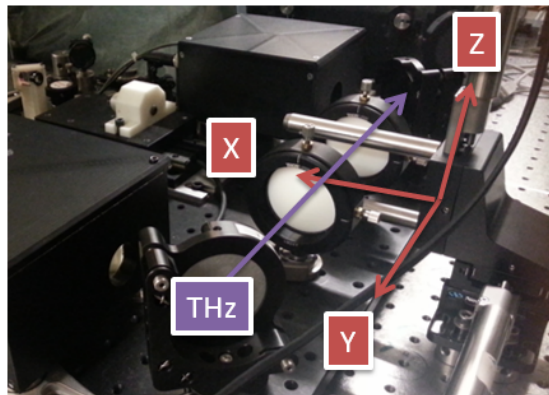


Figure 2.22. Picture of 3-axis motion control stage

Two modes are used for image construction with this system; the fast scan and the regular scan mode. The fast scan mode holds the delay stage at a fixed position (usually in the position providing maximum intensity) and collects a single data point corresponding to the intensity of THz beam. This type of imaging is normally used to identify the beam position by putting a slit which has a hole at the center so that the sample can be correctly located later at that position. Figure 2.23 shows the procedure how to define the beam position in terms of the position of sample holder.

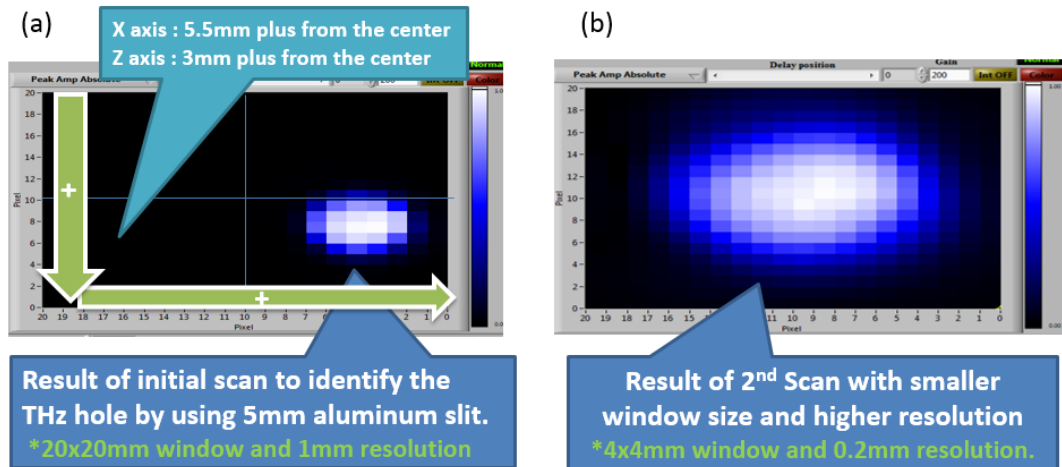


Figure 2.23. Procedure finding the beam position in terms of 3-axis values by performing (a) first scan with maximum (20x20mm) window and (b) second scan with smaller (4x4mm) window

This way also helps the user to define the optimum window size for imaging. Furthermore, this method can build up a three-dimensional image by moving additional axis (y in our system) after finishing and saving a single plane of an image with x and z-axis. This way of imaging especially helps to get the focal point of the two polyethylene lenses as shown in Figure 2.24.

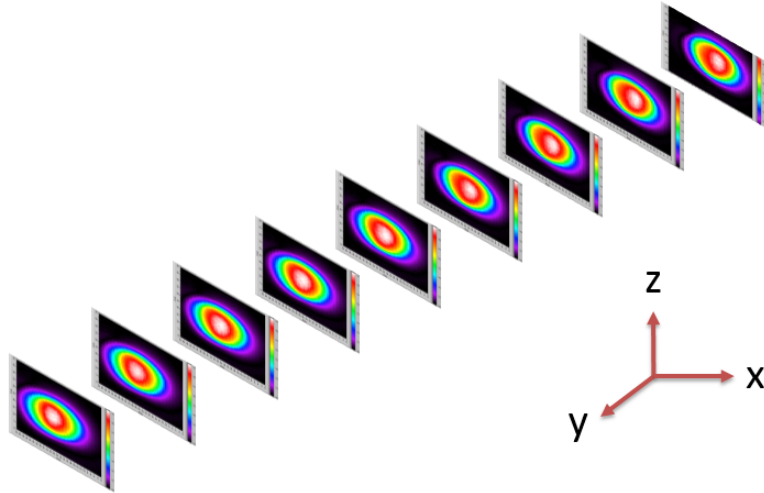


Figure 2.24 Multiple slides obtained by fast mode THz imaging by moving y-axis after building up x-z plane. The white circle at center slightly moves along the y-axis.

The second method, the regular scan mode of image acquisition provides genuine spectroscopic imaging capability. The critical difference from the fast scan mode imaging is, the regular scan allows each pixel to contain the complete spectroscopic information, unlike the fast scan mode. Therefore, regular scanned image can be reconstructed by the filtering the image based on desired frequency-domain signal or even the time-domain signal, so that it can be disclosed meaningful information on its characteristics such as refractive index, material composition and density. Figure 2.25 describes the difference between the two imaging scan modes.

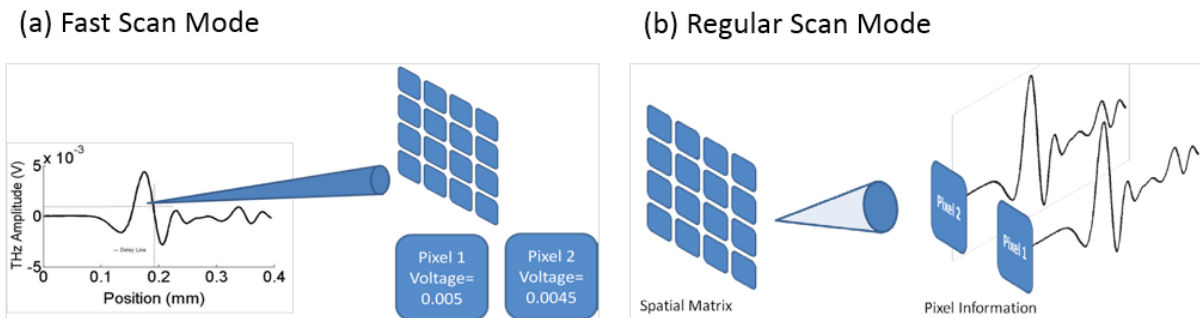


Figure 2.25 Description of (a) fast scan mode and (b) regular scan mode [47]

No matter what, the highlight of the THz imaging is, as it is mentioned in the previous chapter, scanning the biological samples. There was a test performed to reveal an object sealed inside by a paper box during THz imaging. Due to the organic characteristic with respect to the water, a piece of branch with the size of 20mm was identified as shown in Figure 2.26. It shows clear contrast due to the water absorption since the branch was measured within one hour after taken from the original tree.

(a)



(b)

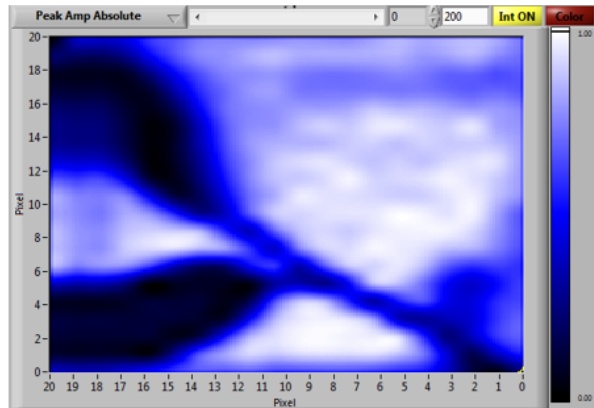


Figure 2.26. THz imaging test of (a) a piece of real organic branch and (b) its imaging result when hidden in a paper box

## CHAPTER 3

### FLEXIBLE METAMATERIAL PERFECT ABSORBERS

#### 3.1. Introduction

Metamaterials hold great promise for improving our ability to manipulate terahertz frequency radiation. Metamaterials typically consist of arrays of subwavelength resonant structures whose size, geometry, and orientation can be selected to allow for exotic optical properties such as a negative permeability or refractive index. Many different metamaterial structures have been proposed [48-51] for applications such as filters [52,53], modulators [54,55], optical cloaks [56,57], and super lenses [58,59]. In particular, the terahertz metamaterial perfect absorber, first reported in 2008 [60], is well suited to a variety of applications due to its high-efficiency operation. However, the incorporation of metamaterials into many of applications will rely on the ability to design and fabricate flexible metamaterial devices.

Although the realization of many advanced flexible electronic devices has only occurred recently, research and development of these types of devices has been ongoing for quite some time. In fact, the first flexible electronic devices were created in the early 1900s for telephone switching applications [61]. Over the past century, flexible device applications have been extended to a broad range of technologies including flexible displays and solar cells as well as in cameras, cellular phones, medical devices, automobiles, and space-based applications such as satellite components. Flexible devices can have many advantages over their nonflexible counterparts. They can be much lighter and smaller when space or weight constraints are critical

and are usually much more durable. One especially advantageous benefit of flexible devices is the ability to be conformed for placement in unusual places and orientations that would be a useful characteristic for metamaterials.

Flexible metamaterials are currently being developed for use in a variety of applications. They are typically fabricated by printing or depositing of resonant metal structures onto a flexible substrate. Results from these types of structures have been shown to exhibit similar functionality in both fixed and flexible forms [62]. Stress/strain sensing applications using flexible metamaterials have recently been realized by exploiting the change in capacitance between the resonant structures during compression [63]. A flexible broadband absorber has also been reported that was composed entirely of flexible Polydimethylsiloxane (PDMS) with no metallic resonant structures [64].

Absorbing a broadband frequency spectrum extremely critical especially in a military application in which already known as stealth technology. Stealth technologies basically allow an object to be partially or fully invisible to specific means of detection. The concept is similar to the camouflage tactics used by soldiers in jungle warfare, but in the modern battlefield, it aims at minimizing all kinds of transmitted and reflected energies - heat, light, sound, electric potentials, etc. - to deny an opponent to locate, track, identify and attack its target. For example, in naval or airborne battlefields, which is the arena of the most advanced scientific technology, it focuses on reducing the detection range or minimizing the reflective RADAR signal. The ability of a vessel or craft to reflect a RADAR signal is called as 'RADAR Cross Section' (RCS). Actual RCS in the battlefield mainly depends on angle of incidence and reflection of the RADAR signals from the surface of the aiming object. Thus, reducing the RCS has been the most important matter while applying stealth technology in the military applications since 'less RCS' means 'less

detectable' by the enemy. There are four widely known methods to reduce the RCS: shaping, RCS absorbent material (RAM), active cancelation, and passive cancelation. Among them, RAM, which absorbs incident RADAR waves, absorbs a particular frequency of RADAR depends upon the composition of RAM as follows; PMCs (Polymer Matrix Composite materials), MMCs (Metal Matrix Composite materials), CMCs (Ceramic Metal Composite materials), Carbon Composites. [65]

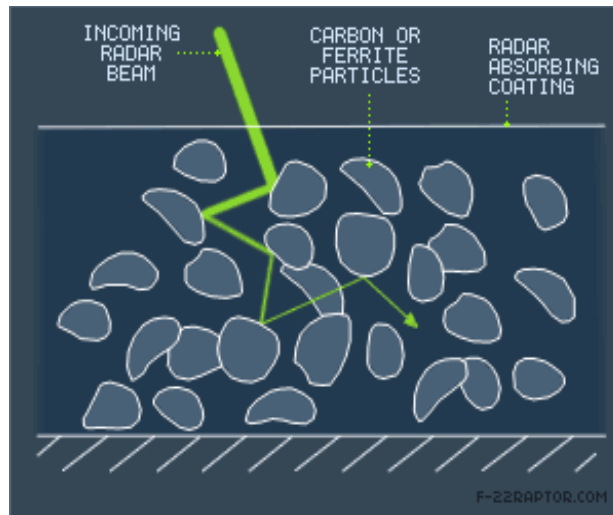


Figure 3.1. Principle of carbon fiber composites as an example of RAM [65]

There also are various types of RAMs already developed and being used depending on the techniques used to absorb the RADAR signals such as 'Iron Ball Paint', 'Stealth nano-carbon paint', 'Foam Absorber', 'Jaumann Absorber', 'Split ring resonator Absorbers'. Although none can absorb all frequencies of RADAR signal, RAM reduces the RCS making the object appears smaller, and all these kinds of efforts for reducing the RCS will definitely help to win the battle.

As one of the new trial for the RAM invention, here in this work, we have focused on flexible metamaterial perfect absorbers (FMPA) using the ring type Frequency Selective Surface (FSS) targeted THz band that were designed through the use of finite element analysis software,

fabricated by standard photolithographic lift-off technique, and characterized with terahertz time-domain spectroscopy (THz-TDS). The major advantage of applying the THz band absorber is that we can minimize the size of resonators down to the micrometer scale instead of the metric scale. The fact that the size of FSS for THz band is comparatively smaller than the one for microwave benefits us to have compact objects that could be miniaturized and experimented inside of lab facilities.

After verifying the thread of connection between the simulation and measurement, we finally focused this measurement on investigating the practical functionality of the FMPA on a variously designed conformal surfaces. That is because we consider it would be used in sensing or cloaking application in a real world, assuming it covers some objects, it has to be robust enough in uneven conditions. The functionality of the structures in both fixed and flexible forms was investigated as well as effects on the resonant response due to variation of the resonant element geometry. This was accomplished through the use of custom sample holders designed to pull the flexible absorbers into conformation with cylindrical or hemispherical surface relief structures.

### 3.2. Design and Simulation

The FMPAs were designed using common three layer approach consisting of a bottom copper ground plane, a dielectric spacing layer, and top Frequency Selective Surface (FSS) layer that was composed of ring resonators. The FSS unit cell consisted of two differently sized, nonconcentric, out-of-plane, circular rings separated by a 1.7 $\mu\text{m}$  thick polyimide dielectric layer as given in Figure 3.2. The ring sizes were selected to target resonant frequencies near 0.75 THz. The unit cell structure was designed such that the larger ring was in the upper layer so that the

resonance of both rings could be easily optimized. A series of four arrays with FSS ring center-to-center spacing (the lateral distance between the centers of the top ring and bottom rings indicated by the parameter  $Lat$  in Figure 3.2) ranging from  $2\mu\text{m}$  to  $8\mu\text{m}$  were simulated at  $0^\circ$  and  $90^\circ$  polarizations to determine the effect of this spacing on the resonant frequencies and absorption strength at each frequency. Table 3.1 summarizes the design parameters for the four different structures.

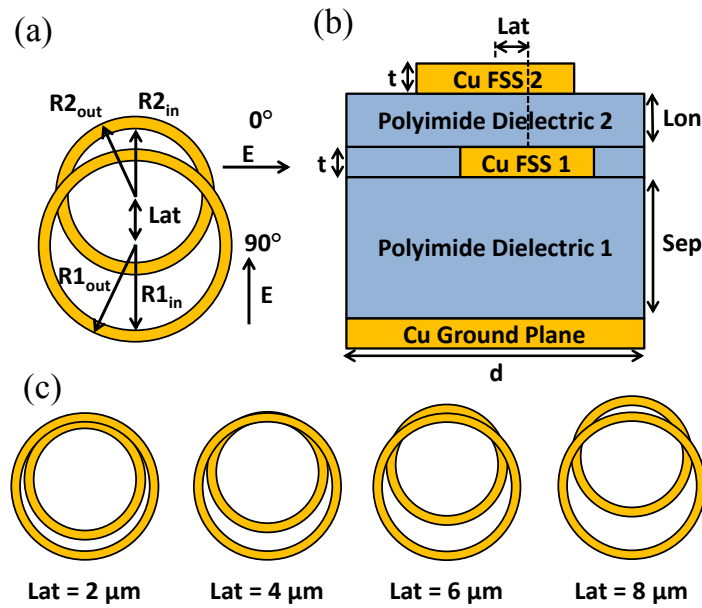


Figure 3.2. Diagrams of the (a) top view of the FSS layer consisting of two nonconcentric rings with labeled incident field polarizations, (b) side view, and (c) center-to-center displacement ring geometries of the flexible absorber unit cell.

	Structure 1	Structure 2	Structure 3	Structure 4
Bottom Ring ( $R2_{in}$ - $R2_{out}$ )	$33\mu\text{m} - 36\mu\text{m}$	$33\mu\text{m} - 36\mu\text{m}$	$33\mu\text{m} - 36\mu\text{m}$	$33\mu\text{m} - 36\mu\text{m}$
Top Ring ( $R1_{in}$ - $R1_{out}$ )	$39\mu\text{m} - 42\mu\text{m}$	$39\mu\text{m} - 42\mu\text{m}$	$39\mu\text{m} - 42\mu\text{m}$	$39\mu\text{m} - 42\mu\text{m}$
Displacement ( $Lat$ )	$2\mu\text{m}$	$4\mu\text{m}$	$6\mu\text{m}$	$8\mu\text{m}$

Table 3.1 Dimensions of bottom ring and top ring with respect to the displacement of the structures. First and second rows give the dimensions of the FSS bottom and top rings, respectively. Third row gives center-to-center displacement (parameter  $Lat$  in Figure 3.2) for each structure.

The simulation models were built based on the listed center-to-center displacements. The constructed unit cell was a total of  $104\mu\text{m}$  square with periodic boundary conditions used to model the FSS array. The nonconcentric nature of the unit cell resulted in a polarization dependent resonant response in the structures as is seen in Figure 3.3. For the  $0^\circ$  polarization, the structure developed a single resonant frequency. The frequency was seen to increase slightly from 0.75 THz to 0.76 THz as the center-to-center displacement of the FSS rings was increased. However, each of the rings shows two distinct resonant frequencies when the electric field was oriented at  $90^\circ$ , along the long axis of the rings, but the two resonant frequencies were close together at 0.74 THz and 0.8 THz. Simulations showed that each ring developed its own strong dipole resonance with the larger ring resonance corresponding to lower frequency at 0.74 THz.

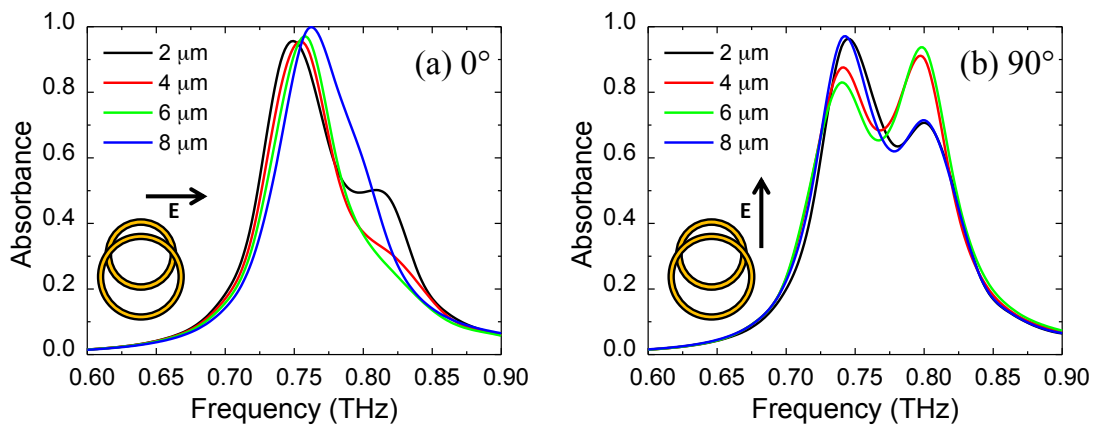


Figure 3.3 Simulated absorbance of the FMPAs at (a)  $0^\circ$  and (b)  $90^\circ$  at varied center-to-center ring displacements given.

The simulation results for the 90° polarization revealed that the absorbance strength at both resonant frequencies was dependent on the center-to-center displacement. The first resonant frequency at 0.74 THz was seen to decrease from 96% at the 2μm displacement before reaching a minimum of 83% at the 6μm displacement and finally increasing back to 97% at 8μm. The second resonant frequency had opposite behavior starting 71% and increasing to 94% at 6μm before returning to 71% at 8μm. These results indicated that the response of the structure to shifting of the unit cell rings could be exploited for sensing applications based on the center-to-center displacement.

### 3.3. Experimental Procedure

The fabrication of the flexible absorbers began with the application and curing of a 10.7 μm thick layer of polyimide (HD-MicroSystems PI-2610) on a 3” diameter sacrificial Si wafer by spin coating and curing hard bake at 350°C for 30 min. This polyimide layer would serve as the flexible substrate. The metal ground plane consisting of a 15 nm Cr adhesion layer and 185 nm Cu layer was deposited onto the polyimide substrate by electron beam evaporation (E-beam) deposition. An additional 10.7μm thick layer of polyimide that would make up the dielectric spacer layer was applied to the metal ground plane. Next, a 250 nm thickness SiO<sub>2</sub> layer was deposited which would be the first part of the SiO<sub>2</sub> encapsulation of the first FSS layer. A thin layer of positive photoresist was applied on the SiO<sub>2</sub> layer by spin coating. The photoresist was then exposed through a dark-field photomask in order to pattern the first FSS layer rings with ion beam etching used to etch the ring patterns to a depth of 200 nm into the SiO<sub>2</sub>. This was followed by E-beam deposition (15 nm Cr/185 nm Cu) of the first FSS layer rings and subsequent lift-off process. The SiO<sub>2</sub> encapsulation was completed with a 50 nm thick SiO<sub>2</sub>

deposition. Then a 1.7 $\mu\text{m}$  thick layer of polyimide was applied and hard baked to serve as the dielectric spacer between the two FSS layers. Finally, the second FSS layer of rings was patterned by duplicating the UV photolithography process used for the first FSS layer rings, followed by another 15 nm Cr/185 nm Cu E-beam deposition and subsequent lift-off process. The finished flexible absorbers could then be removed from the sacrificial Si wafer. The fabricated structures were inspected by optical microscope between fabrication steps as well as after completion to evaluate FSS ring uniformity. Figure 3.4(a) shows an optical microscope image of a fabricated FMFA corresponding to 6  $\mu\text{m}$  center-to-center displacement.

Characterization of the fabricated structures by reflection mode THz-TDS was performed both before and after removal of the flexible absorbers from the sacrificial Si wafer. A photoconductive antenna emitter pumped with a 780 nm ultrafast (120fs pulse width, 76 MHz repetition rate) laser was used with electro-optic sampling detection in the THz-TDS system. A three-dimensional motion controlled stage was used to position the flexible absorbers in the terahertz beam path. Measurement of the response of the structures to deformation required a unique method for deforming the absorbers. This was accomplished through the use of two custom designed vacuum holders that had a recessed region, shown in Figure 3.4(d), which could be evacuated when covered by the flexible absorbers. The area in this recessed region was populated with an array of surface relief structures in the form of half-cylinders or hemispheres, given in Figure 3.4(b) and (c), respectively, to which the flexible absorber would conform when under vacuum. The holders were produced by 3-D printing.

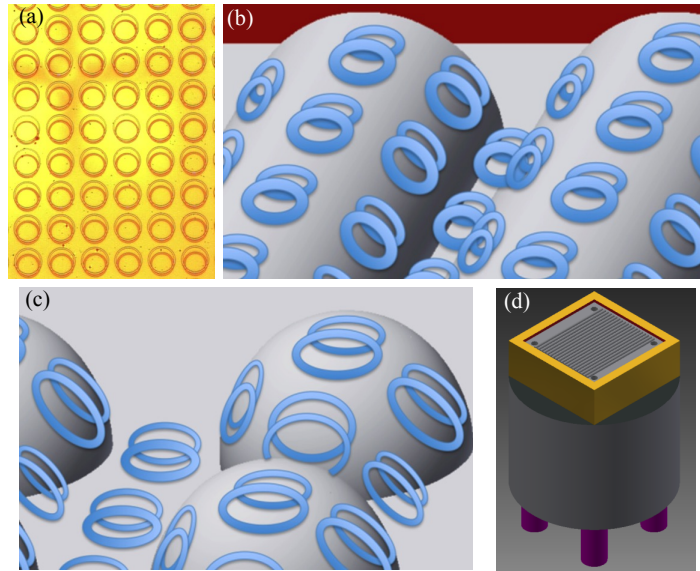


Figure 3.4 (a) Optical microscope picture of fabricated FMPA with  $8\mu\text{m}$  center-to-center displacement. Diagrams of the (d) deformation vacuum holder design with device conformation to the (b) cylindrical and (c) spherical surface relief structures.

### 3.4. Results and Discussion

Analysis of this device has been done based on multiple factors such as resonant frequency, absorbance at targeted frequency in accordance with the surface shape, and the orientation of different polarization angle of the electric field to make this measurement unique. First of all, the result measured from the fixed device on the flat Si surface, before separating the flexible film from the parental wafer, showed the same pattern of graph with the simulation result in terms of ‘resonant frequency transition’ depending on the ‘displacement of the rings’ as shown in the Figure 3.5(a) and (b). Although the resonance frequency of measured one shows approximately 10GHz lower than the simulation, this tendency lets us say the fabrication of the device was quite meaningful.

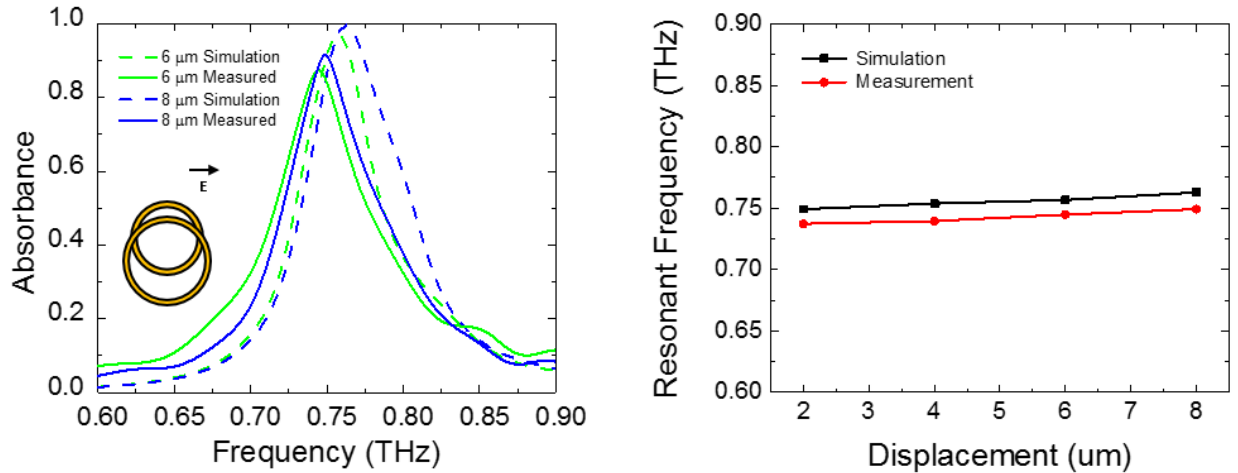


Figure 3.5 (a) Simulated and measured absorbance of the FMPAs for fixed one on a parental Si wafer when the center-to-center ring displacements was  $6\mu\text{m}$  and  $8\mu\text{m}$ , and (b) measured change in resonant frequency as a function of center-to-center ring displacement at  $0^\circ$  E-field polarization.

The measurement of separated device from the Si wafer, which is now flexible but in a flat condition also shows kind of similar results to the simulation as shown in Figure 3.6. The most notable thing in this figure is the existence of second resonance peak around 0.8 THz for both  $0^\circ$  and  $90^\circ$  E-field polarization. For example, in  $0^\circ$  polarization, only  $2\mu\text{m}$  one had second resonance around 0.8 THz in both measured and simulated one. In  $90^\circ$  polarization, even though the second resonant peak is not obvious as the simulation of  $4\mu\text{m}$  and  $6\mu\text{m}$  one, the absorbance of  $4\mu\text{m}$  and  $6\mu\text{m}$  ones are higher than the  $2\mu\text{m}$  and  $8\mu\text{m}$  ones in both simulation and measurement results. In addition, the shapes of absorbance of  $2\mu\text{m}$  and  $8\mu\text{m}$  ones are pretty similar each other. To sum up, the device is similarly performing as we expected except undistinctive second resonant peak at  $4\mu\text{m}$  and  $6\mu\text{m}$  displacement in a  $90^\circ$  polarization measurement.

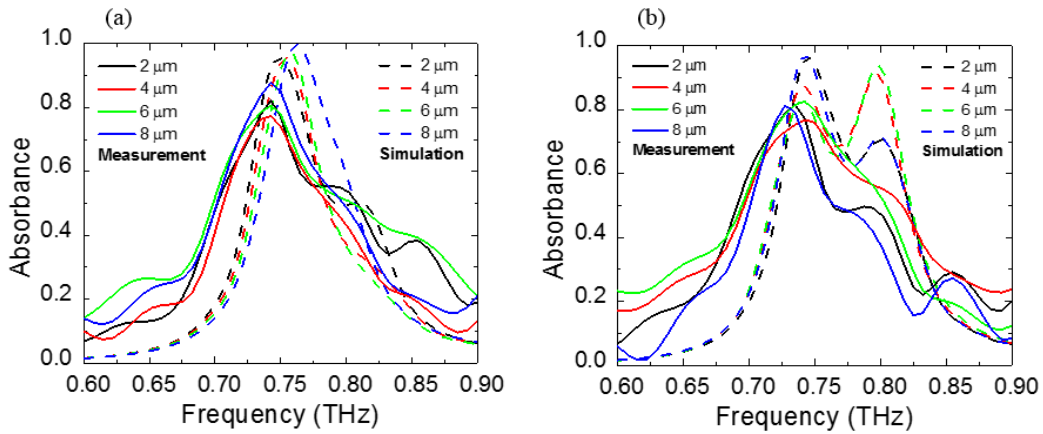


Figure 3.6. Measured and simulated absorbance of the FMPAs on a flat surface at (a) 0° and (b) 90° at varied center-to-center ring displacements.

As mentioned above in the introduction, to verify the robustness of this device with respect to the multiple surface relief structure, the absorbance at the resonant frequency on cylindrical, hemispherical and pyramid surface as shown in Figure 3.7 had been investigated.

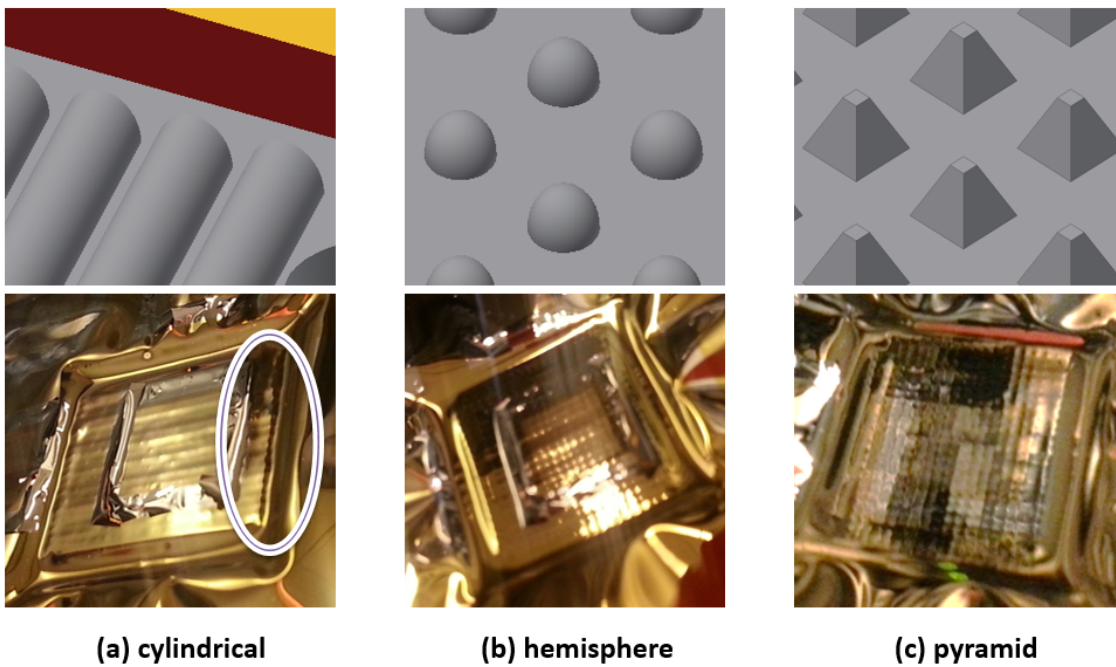


Figure 3.7. Pictures of deformed flexible device on a (a) cylindrical (b) hemispherical (c) pyramid shape of custom holders by using vacuum force.

The results from each deformed surface showed the same trend of the resonant peak just like the flat surface, within the error range of frequency as shown in Figure 3.8. Compare to a flat surface, the response from the conformal surface shows less broadening. In addition, absorbance strengths do not change compared to the flat surface.

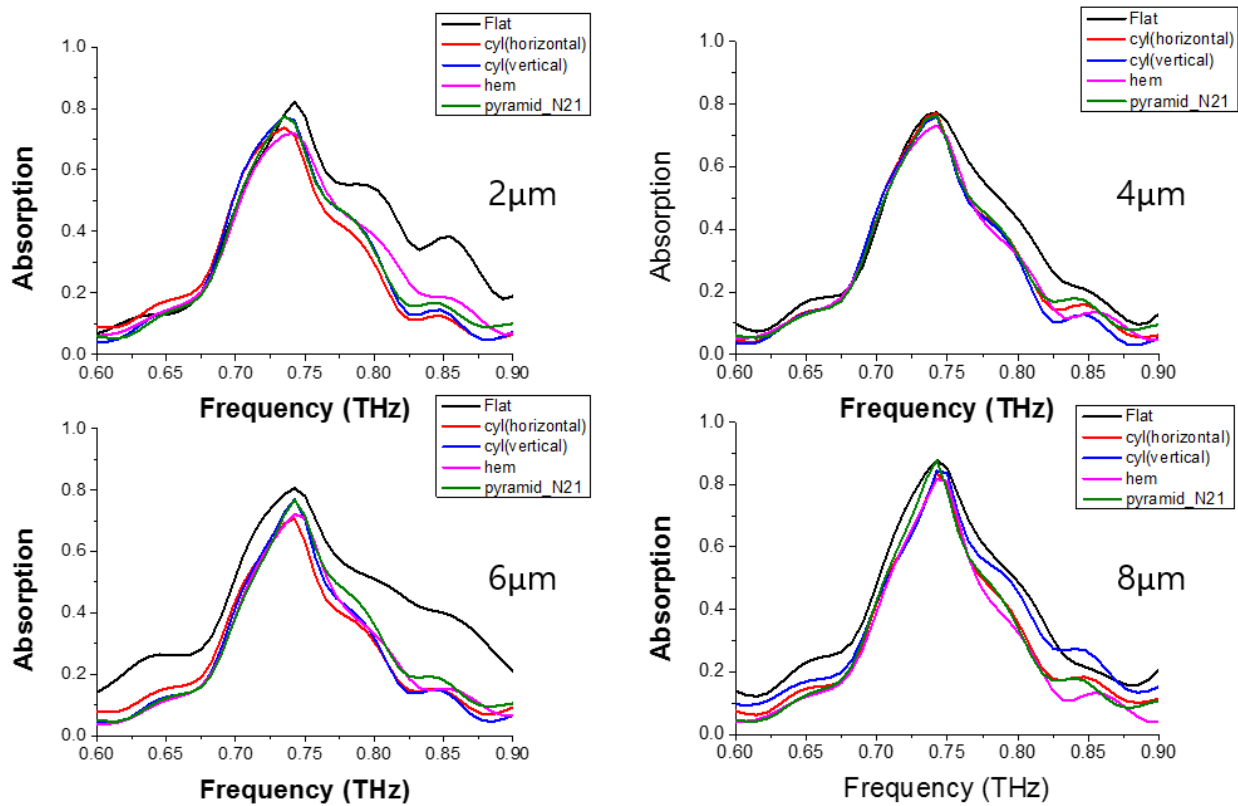


Figure 3.8. Measured absorbance of the FMPA on a various type of surface at 0° E-field polarization.

For further comparison, we have collected all the peak value of absorbance at the resonant frequency and plotted as a function of shape as shown in Figure 3.9. It is observed that the cylindrical and hemispherical shapes seem more sensitive than the flat and hemisphere. Even under the deformation, pyramid shape was more robust. In terms of center to center distance of

the FSS, unlike 8 $\mu\text{m}$  one, 4 $\mu\text{m}$  and 6 $\mu\text{m}$  ones show relatively sensitive response according to the result shown in Figure 3.9.

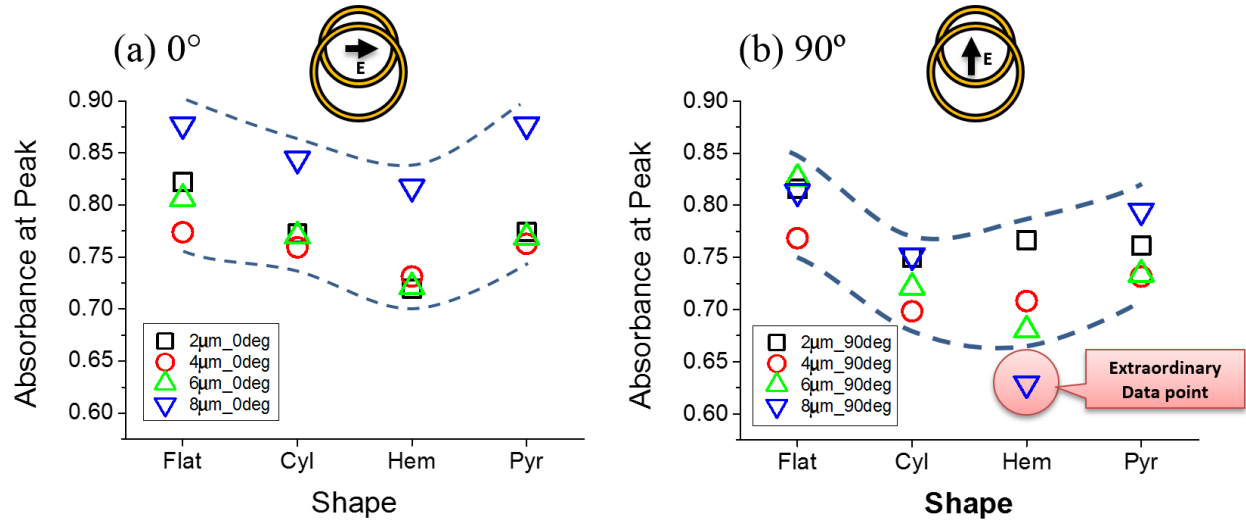


Figure 3.9. Absorbance at resonant frequency as a function of shape in (a) 0° and (b) 90°.

The most interesting thing is, the device which has 8 $\mu\text{m}$  of center-to-center ring displacement had approximately 10 percent more absorbance than the other ones in 0° polarization measurement while 8 $\mu\text{m}$  one was not dominant in 90° polarization measurement. In addition, a trend such that higher absorbance of flat and pyramid surface than the ones of cylindrical and hemispherical surface was identified in both polarization angle. In the meantime, the measured absorbance at a resonant frequency in 90° polarization are generally less than the ones measured in 0° polarization. However, in general, it still follows the same trend of 0° polarization measurement. In summary, in spite of a little reduction of absorbance in 90° polarization measurement, this result supports the purpose of this measurement such that the device as an absorber carries out its function well in a variety of rough surfaces.

### 3.5. Summary

In this work, I have reported FMPAs that were designed, simulated, fabricated through a photolithographic lift-off process, and characterized by reflection mode terahertz time-domain spectroscopy. The structure consisted of a metal ground plane, a polyimide dielectric spacer, and a FSS composed of two layers of nonconcentric, differently sized, circular ring resonators. We showed by simulation and verified by measurement that the FMPA resonant response is dependent on the center-to-center displacement of the FSS unit cell rings which could be exploited for sensing applications. Additionally, the functionality of the FMPAs in fixed and flexible forms, as well as while under deformation, was evaluated and found to be consistent and robust. This result could lead to future applications in cloaking since this FMPA showed enough robustness when it covered another object whose surface is rough and uneven.

## CHAPTER 4

### INVESTIGATION OF BREAST EPITHELIAL LINE USING THZ-TDS

#### 4.1. Introduction

As I mentioned in chapter 1, implementation of radiation at Terahertz frequency can yield great advancements in the wide fields of industries especially for the biomedical engineering. Especially, the observable vibrational modes of most molecular bonds at THz frequency and its fingerprint regions on organic compositions and water vapor strongly contributed these kinds of expectation for biological sensing and imaging. Also, the THz wave is non-ionizing, which means its photons are not energetic enough to knock the electrons of atoms and molecules in human tissue. Thus, it cannot trigger any harmful chemical reactions unlike X-ray, and it can penetrate many non-conductive materials harmlessly, such as plastics and clothes while letting spectroscopic probing of target objects behind the blocking materials. [66] With these characteristics, the THz pulse method, represented by THz time-domain spectroscopy, became a unique characterization technique for sensing organic compounds such as tumors, narcotics, and explosives. [67-72]

As the THz-TDS technique developed, numerous THz imaging methods also have been developed from the first THz imaging exhibited in 1995 [73]. After the last 20 years of booming interests and tremendous efforts of scientists from all over the world, terahertz spectroscopic imaging is now expected to become a strong candidate for safe in-vivo biomedical imaging such as cancer tracking, wound assessment, burn diagnosis [74], tooth caries and skin cancer detection

[73], and normal and cancerous biological tissue imaging [74,75]. Most of these advancements were achieved by utilizing the Terahertz pulsed imaging (TPI), which uses transmission or reflection mode of THz-TDS.

Among them, we are interested in the recent researches utilizing THz spectroscopy in distinguishing various breast tissues such as healthy fibrous breast tissue, healthy adipose tissue, and breast cancer [77]. These advancements in THz spectroscopy have even led to the creation of new and improved intra-operative tools to distinguish breast cancer tumor margins [77]. While there are studies done on distinguishing breast tissues *ex vivo* and even *in vivo* using THz, it is evident that there is very little research done on breast cancer cell lines itself. As a result, the goal here is to study the interactions of THz radiation on cancer cell cultures instead of tissue cultures and be able to characterize and identify the cells. By monitoring the cells, real-time, as they transition from their active (in the presence of the media) to inactive state (as the media dries out), there may be features in either state that can lead to identifying the cells.

If a cell identification technique using THz can be established, it will be useful to characterize and identify cells at laboratories and research institutes that mass produce cell lines. The real-time monitoring of cell lines can also open a window towards studying the effects of various environments such as drugs, pH, temperature, etc. on them. Furthermore, in Ashworth et al.2009, the breast tissues are distinguished by determining their respective refractive indices and absorption coefficients, however, the cause of this uniqueness in their optical properties is not understood [77]. Studying the cell lines could also unveil the reason behind the changes in the optical property of the tissue samples.

## 4.2. Experimental Procedure

### 4.2.1. Sample Culturing

Both breast normal cells and cancer cells were cultured by our collaborator from the Chemical and Biological Engineering Department of the University of Alabama. Here, I briefly mention how it is cultured.

The breast tissue cell line 184A1 (ATCC, Manassas, VA) was cultured in Mammary Epithelial Basal Medium (MEBM) (Lonza) supplemented with 1% penicillin/streptomycin (Corning, Manassas, VA), 0.005mg/mL transferrin and 1 ng/mL cholera toxin. The breast cancer cell line MDA-MB-231 (ATCC) was cultured in phenol-red free Dulbecco's Modified Eagle's Medium (DMEM) (Gibco, Grand Island, NY) supplemented with 1% L-glutamine (Life Technologies, Carlsbad, CA) and 10% Fetal Bovine Serum (FBS) (Gibco). Both cell lines were cultured using the recommended protocol by ATCC in Poly D-Lysine 35mm dishes (Benton Dickinson, Bedford, MA) as shown in Figure 4.1.

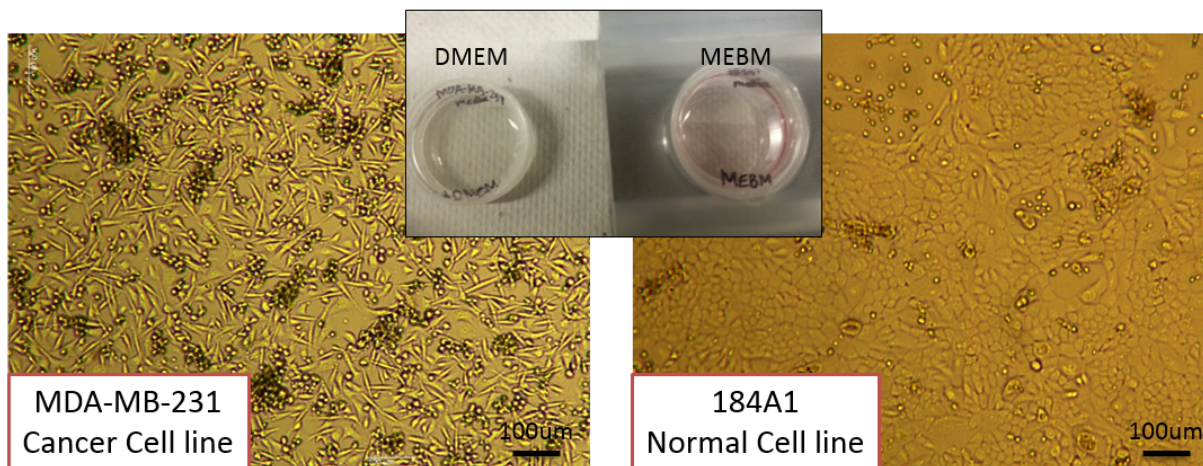


Figure 4.1 Microscopic Images of the (a) MDA-MB-231 Cancer cells in the growth media DMEM and (b) 184A1 Normal cells in the growth media MEBM

#### 4.2.2. Measurement preparation

THz scan was performed over each sample under the transmission mode of THz-TDS. As shown in Figure 4.2, a 3D-printed custom holder was used to hold the sample-grown dish and to tilt it at an angle of 90 degrees. The 90-degree tilting was performed to drain out the media because the media, as a liquid, absorbs most of THz radiation as shown in Figure 4.3.

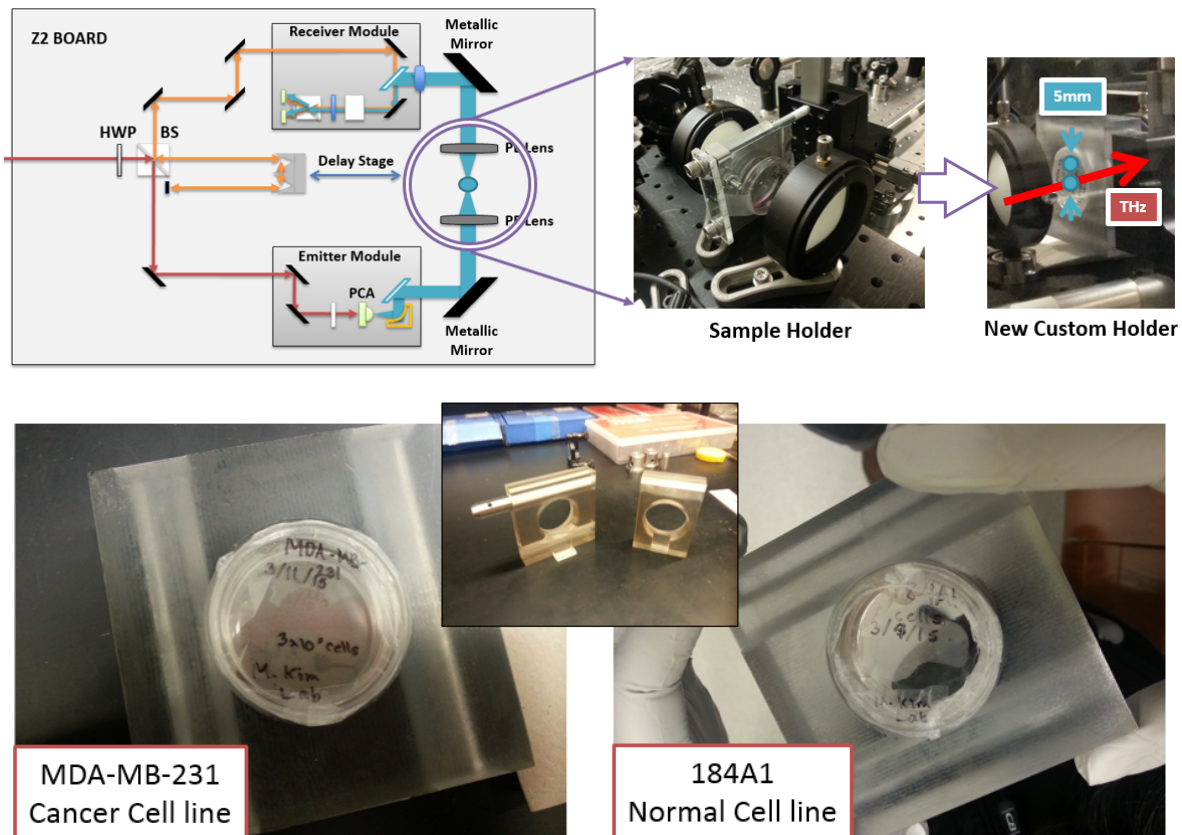


Figure 4.2 Diagram of Transmission mode TDS and the pictures of the sample stages.

Both measurements were conducted in purged condition. It was purged with nitrogen gas ( $N_2$ ) during the scan to minimize any absorption due to the moisture since multiple water vapor absorption lines exist in the spectral region around 1.09 THz and 1.72 THz. Poly D-Lysine 35mm dishes without cells measured in advance as a reference. The measurement was performed in two phases; without sealing and sealing the dishes. The first measurement was performed

without sealing, so most of the media was leaked out. After that another measurement was performed with sealing to verify the difference between spectroscopic response and affection of sealing the dishes. The dish was sealed by the ‘Parafilm M’ laboratory film, which is a moisture-resistant thermoplastic, to prevent leaking of media.

In order to also monitor the real-time changes in the sample, the scans were repeated every 8 minutes. This was done twice on each sample to normalize the result; first, at the center of the dish and then at 5mm off the center. Lastly, scans were performed on the negative controls which are the growth media used for the respective cell cultures. The negative control helped to rule out any peaks stimulated by the media itself.

#### 4.3. Results

The transmission ratios for each of the scans were plotted by dividing the results from the samples by the results from the reference (sample holder by itself). The plots showed that though the negative controls absorb considerable amount of THz signal there are no distinguishable peaks as shown in Figure 4.3, implying that the transmission ratios of the cell cultures are solely due to cell-cell or cell-medium interactions.

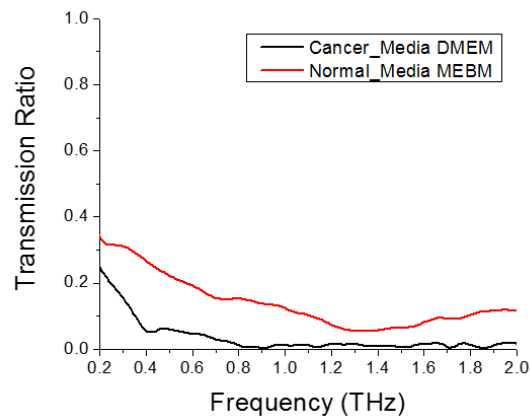


Figure 4.3 Transmission ratio of the both media for cancer cells and normal cells as a negative control measurement

Exploring the frequency domain also was performed with two phases depending on the sealing the dishes. In both cases, similar peaks were seen, and the peaks disappeared with time flow due to drying out of the media. Both cell lines displayed similar peaks, and a clear time variation was seen between them as shown in Figure 4.4 and 4.5. Measurement performed without sealant film around the dishes induced to be hardly dried so that there was no any moisture inside of the dish after drained out of the media. Figure 4.4 shows the spectroscopic result of both cancer cell and normal cell lines as if there is nothing on the dishes to be characterized after a few minutes. This motivated me to seal the dishes so that the humidity inside of the dish could be constant during the measurement.

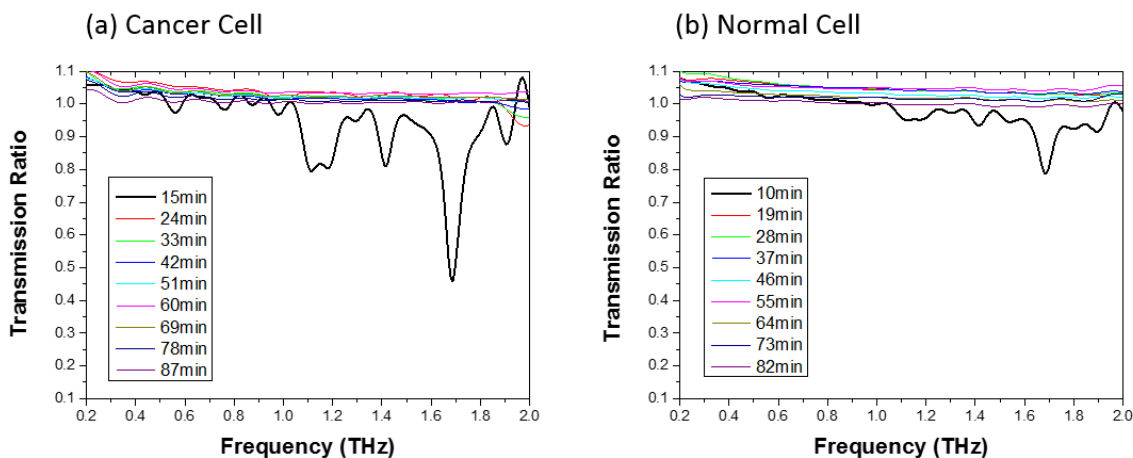


Figure 4.4 Measurement result of (a) cancer cell line and (b) normal cell line in purged and non-sealed condition

The second phase of measurement with sealing the dishes provided an interesting result as shown in Figure 4.5. A time variation still could be observed clearly, and most of all, there was a distinct peak that differentiate the normal cell from cancer cell around 0.4 ~ 0.45THz. Upon further investigation of the molecular level interactions, we should be able to decipher the reason for this variation and ascertain a method to identify the two cell types.

The spectrum for both of the cancer cell and normal cell at 9 minutes showed that the cancer cell peaks disappear in a similar speed with respect to the normal cells. In addition, somehow the transmission ratio has a characteristic such that it has a tendency to have a symmetric peak with the course of time.

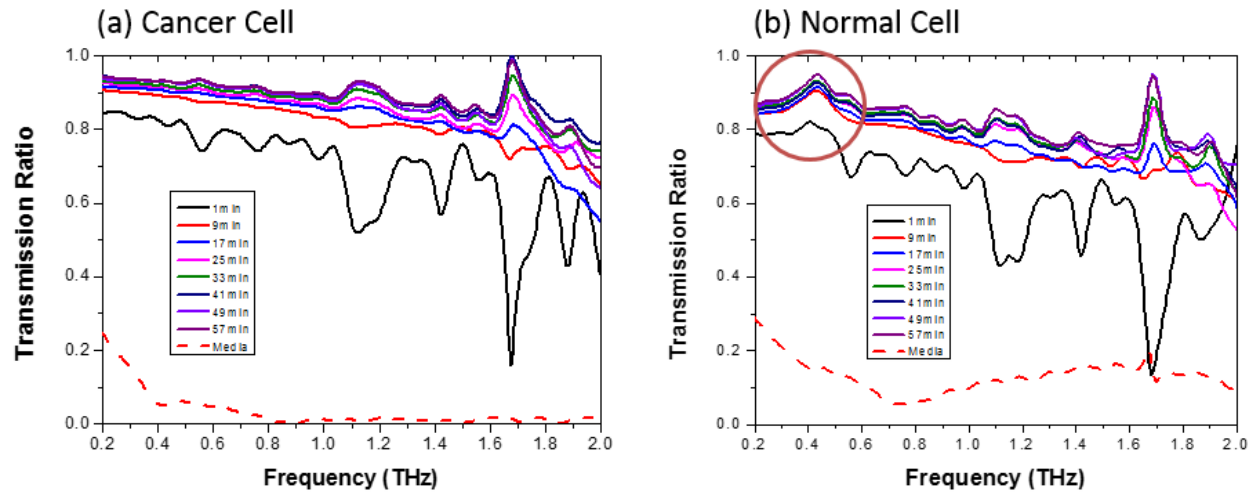


Figure 4.5 Measurement result of (a) cancer cell line and (b) normal cell line in purged and sealed condition

Additional measurement performed with dead normal cell lines verified the fact that there is a characteristic such that the transmission ratio graph becomes horizontal straight line along the x-axis when the cells are dead unlike living cells that have a slope as shown in Figure 4.6. Dead cells were obtained by leaving them in the room temperature for one week so that they could die due to the lack of nutrition. The reason the slope disappears in the dead cell is directly related to the way we executed this measurement. When we tilt the dish in 90 degrees so that the media was pooled the down by gravity, the living cells have more tendency to hold and to contain the media as a natural metabolism. On the other hand, the dead cells have no ability to react to the changing circumstances. Thus, the final parallel straight lines which represent 100% transmission ratio along the x-axis in Figure 4.6 could be clarified as dead cells.

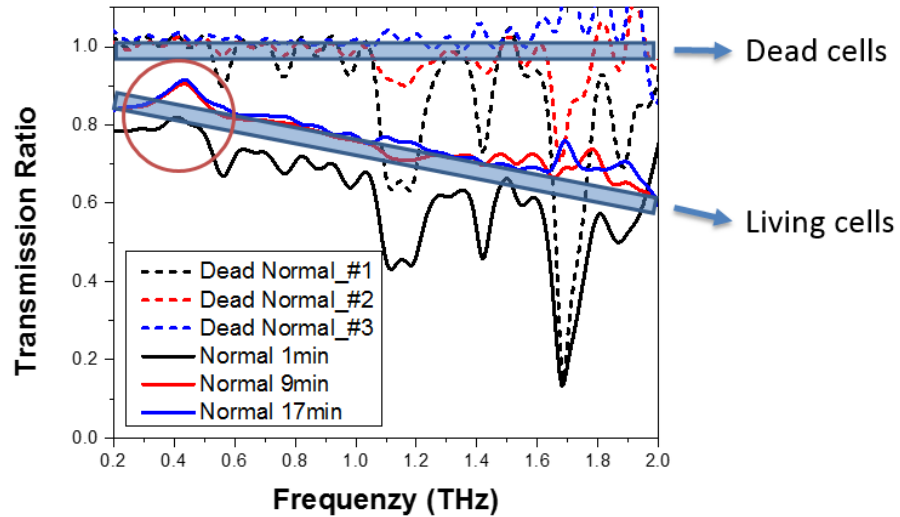


Figure 4.6 Difference in transmission ratio of living cells and dead cells using THz-TDS spectroscopy

#### 4.4. Summary

This measurement was the first trial for the living human breast cells in our laboratory. The two comparable object; the normal breast cell and the cancerous breast cell was used to be characterized. Under the purged condition by providing excessive nitrogen gas (N<sub>2</sub>), when the samples were not sealed, all the medium leaked out from the dishes. The effective response of result in this case was limited to only the first scan. The other scans displayed nothing as if there are no organic features. On the other hand, the second case with the sealant film around the sample dish showed us significant difference from the frequency domain analysis with distinct peak information. Although the result showed unique peak only from the normal cell around 0.4THz in the frequency domain, I strongly believe that this result is meaningful enough to be exploited for the future cancer cell and normal cell discrimination. Furthermore, additional measurement targeted for the dead cell also displayed clear difference with the living cell in terms of transmission ratio along the THz frequency. Understandably, the further measurement will be needed to develop this result and to verify the reason and principle of this phenomenon.

## CHAPTER 5

### THZ EMISSION FROM NANOWIRES

#### 5.1. Introduction

Picosecond optoelectronic switching, which was later named as a photoconductive antenna (PCA), has been the most conventional method for THz generation since the 1970s when it was first introduced [78]. Due to its controllable lifetime by the substrate temperature in epitaxial growth by molecular beam epitaxy (MBE), the most common THz emitter is known as low temperature grown GaAs (LT-GaAs) PCA which actually requires a high voltage bias. Recently, researchers have been looking for a good candidate for unbiased THz emissions to replace PCAs as an emitter because it will be a simpler and compact set-up if we do not use a high voltage bias which occupies a large space. Although the THz band has a variety of benefits for the future applications, it will never be practical without miniaturizing the THz setup. In that point of view, obtaining the THz source without the biasing device will be a significant one step forward the breakthrough.

From the early 1990s, we have known that THz waves can be generated from semiconductor wafer surfaces under the illumination of femtosecond optical pulses which excite the surface with an oblique angle (usually  $45^\circ$  relative to the normal) [79]. As the dimension of the material changes from wafer to an array of nanowires (NWs), under the same ultrafast laser spot size, the total effective surface area drastically increased and resulted in a higher absorption which will play an essential role for enhanced THz emission intensity. There have been reports

investigating the THz emission from a variety of semiconductor NWs, and one of these enlightening studies has been done on Ge NWs showing that THz pulse intensity emitted from Ge NWs is significantly higher than that emitted from Ge wafer [80]. Here in this measurement, multiple combinations of semiconducting  $\text{Si}_{1-x}\text{Ge}_x$  NWs were prepared and tested to verify that effectiveness of Ge contents in the NWs.

In addition, as a different approach to the fabrication of NWs, unlike all the NWs samples that have been prepared by growth processes such as vapor phase epitaxy, chemical vapor deposition, we suggested fabricating the NWs by e-beam lithography which we can achieve excellent vertical alignment and perfectly uniform distribution with desired diameter and length. Growing is not the best method to prepare the NWs due to lack of control on the structural geometry of the wires, e.g., aspect ratio, vertical alignment, and uniform distribution. InP and InGaAs NWs were fabricated using the new method and tested in this chapter.

## 5.2. Experiment Procedure

### 5.2.1. Measurement Setup

For this measurement, a conventional pump-probe method with ultra-femtosecond pulsed laser was utilized. Setting up the optical components for this THz emission test was quite tough due to the optical alignment. As of the surface emission method, unlike the PCA emitter that generates directional THz wave, THz wave would be randomly scattered from the NWs if there were no enclosures. Thus, the best way to utilize the surface emitter is known as putting them in 45 degrees from the incident laser beam so far. [79] However, collecting the reflected THz wave is again a matter since it is pretty hard to cover every direction of emitter source due to the reflective and diffusive characteristics of electromagnetic waves. To minimize the loss of emitted

THz waves, we have used a pair of off-axis parabolic (OAP) mirrors as shown in Figure 5.1. The chopper was also equipped to modulate the frequency of input laser pulse at 2.4 kHz. Another combination of the beam splitter and half wave plate was equipped to control the power of the input laser pulse since the first combination has to control the power of probe side laser beam. The second combination of the beam splitter and half wave plate helped to control the input power for the NWs and to measure polarization dependent measurement that will be discussed in the result part.

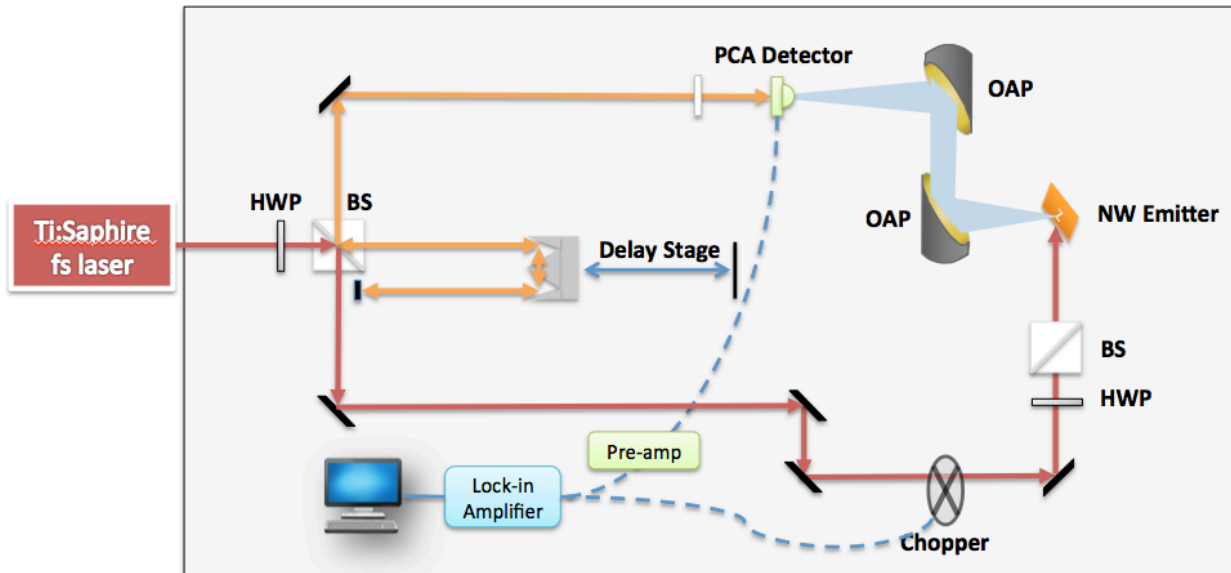
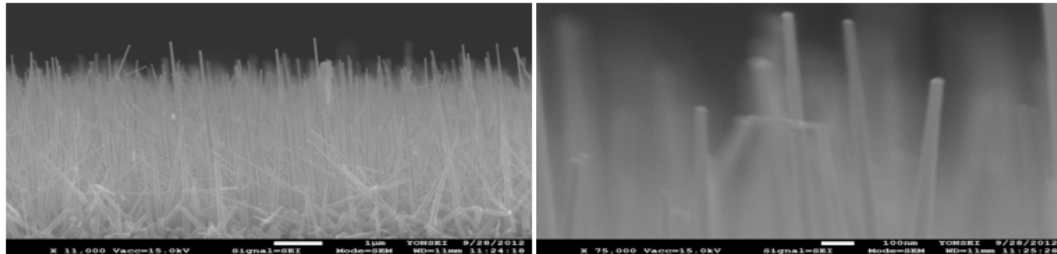


Figure 5.1. Diagram of setup for THz emission test from NWs

### 5.2.2. Samples Fabrication

Multiple combinations of semiconducting  $\text{Si}_{1-x}\text{Ge}_x$  NWs, which were fabricated by our collaborator were first prepared as shown in Figure 5.2. [80]



Sample	$\text{SiH}_4$ (sccm)	$\text{GeH}_4$ (sccm)	Wire length ( $\mu\text{m}$ )	Ge contents(at.%)
#1	18	2	6.5	29.48
#2	16	4	6.5	36.87
#3	13.33	6.67	6.5	51.92
#4	10	10	5.5	78.73
#5	6.67	13.33	5.5	84.28

Figure 5.2. SEM images of the  $\text{Si}_{1-x}\text{Ge}_x$  nanowire samples and its composition ratios

These SiGe NWs were first implemented to test and build up the optical setup for the entire measurement. Our further investigation using the InP and InGaAs nanowires was motivated from the working with these nanowires.

For the InP and InGaAs sample regarding etching them using E-beam lithography, the fabrication process began with bare wafers.  $\text{SiO}_2$  was deposited on the wafers by PECVD following with spin coating of the resist layer. To etch the shape of NWs, first E-beam was exposed to write the mask of NW patterns. It was followed by the development of the HSQ (Hydrogen silsesquioxane) resist. Through a plasma etching process and removal of the resist by HF (Hydrogen Fluoride), we could achieve perfectly aligned NWs which were distributed exquisitely uniform along the wafer with a fixed pitch length in both x and y-axis as shown in Figure 5.3.

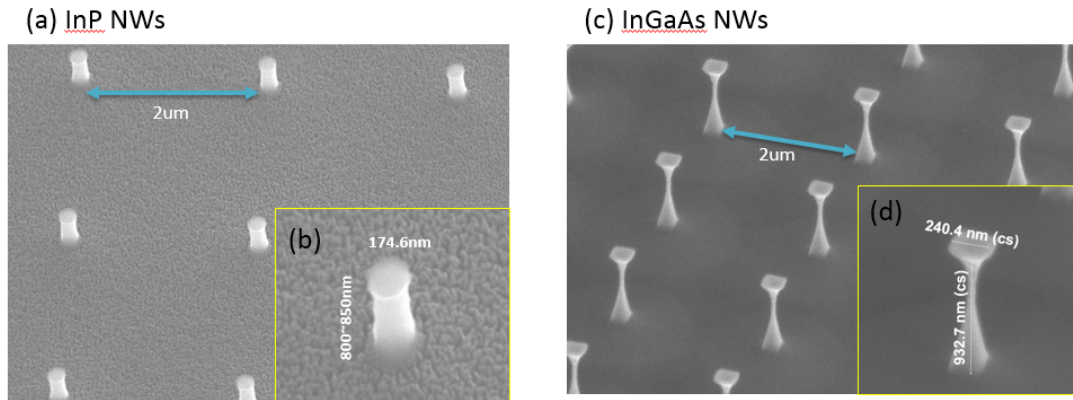


Figure 5.3. (a) Low-magnification SEM image of the InP nanowire arrays showing the perfect uniform distribution of the wires with a  $2\mu\text{m}$  of fixed pitch length. (b) Higher-magnification SEM image which shows the dimension of each NWs. (c) Low-magnification SEM image of the InGaAs nanowire arrays. (d) Higher-magnification SEM image of InGaAs which shows the dimension of each NWs.

### 5.3. Results and Discussion

First measurement result regarding the  $\text{Si}_{1-x}\text{Ge}_x$  NWs are as shown in figure 5.4(a) and (b). These figures clearly show the increasing trend of peak intensity as the Ge contents become higher. The peak to peak value comparison also calculated to show the linearly increasing trend depending on the increasing Ge contents.

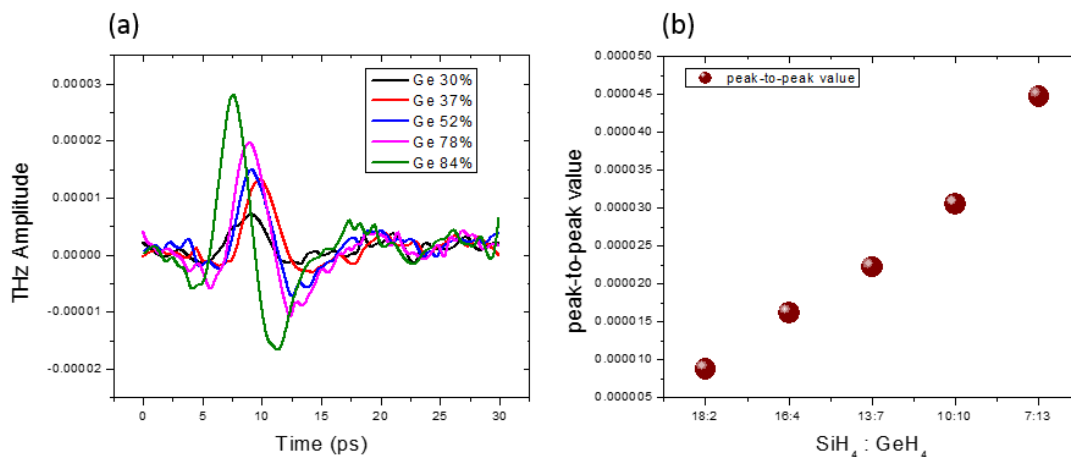


Figure 5.4. (a) Measurement in time-domain graph comparing the THz amplitude detected by different combination of SiGe NWs and (b) comparison of peak to peak value for the measured time-domain signals

Second measurement result regarding the InP and InGaAs NWs are as shown in Figure 5.5. In addition to the nanowires, their parental wafers were also measured to show how the NWs affect the intensity of emitted THz wave. The result of SiGe NWs #5 was also added in this Figure to compare the amplitude of THz wave depending on the semiconductor materials. The result showed that the InGaAs NWs are a better candidate for Surface NW emitter due to its conspicuous amplitude. Each result from InP and InGaAs NWs clearly displays that the amplitudes of NWs are higher than those of their parental wafer in both materials as we intended.

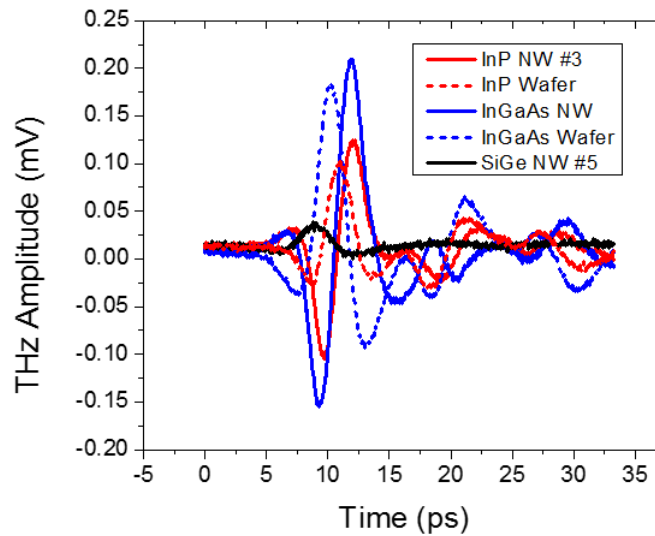


Figure 5.5 Overlapped amplitudes of emitted THz from InP/InGaAs NWs and their parental wafers

Another measurement was performed to investigate how the NWs respond to the two different linear polarizations: p- and s- polarization as shown in Figure 5.4(a) and (b). One clear thing is, the variation of the p- and s- polarization of InGaAs NWs is way larger than that of InP NWs.

For this interpretation, virtual NW diagrams of each sample are added below the Figure 5.4(a) and (b). The arrows on the NWs indicate the direction of the coherent surface plasmon motion under each polarization. If you remind the shape of each NWs from the Figure 5.3, the width of single NW in InGaAs sample were much thinner than that of InP sample. In addition, the length of single NW pole in InGaAs (932nm) also a little bit longer than that of InP (about 800~850nm). Therefore, we conclude that fabricating longer and thinner NWs promises more polarization sensitive NWs for the terahertz radiation.

Another thing clearly clarified is that, for the most efficient THz emission from those thin and long NWs, the NW ensemble should be excited by the p-polarized femtosecond laser pulse. As you can see from Figure 5.6(b), the p-polarized emission is almost twice stronger than the s-polarized emission. In this case, the emission would oscillate the charges along the wire, resulting in a THz radiation in the direction of the surface normal of NWs.

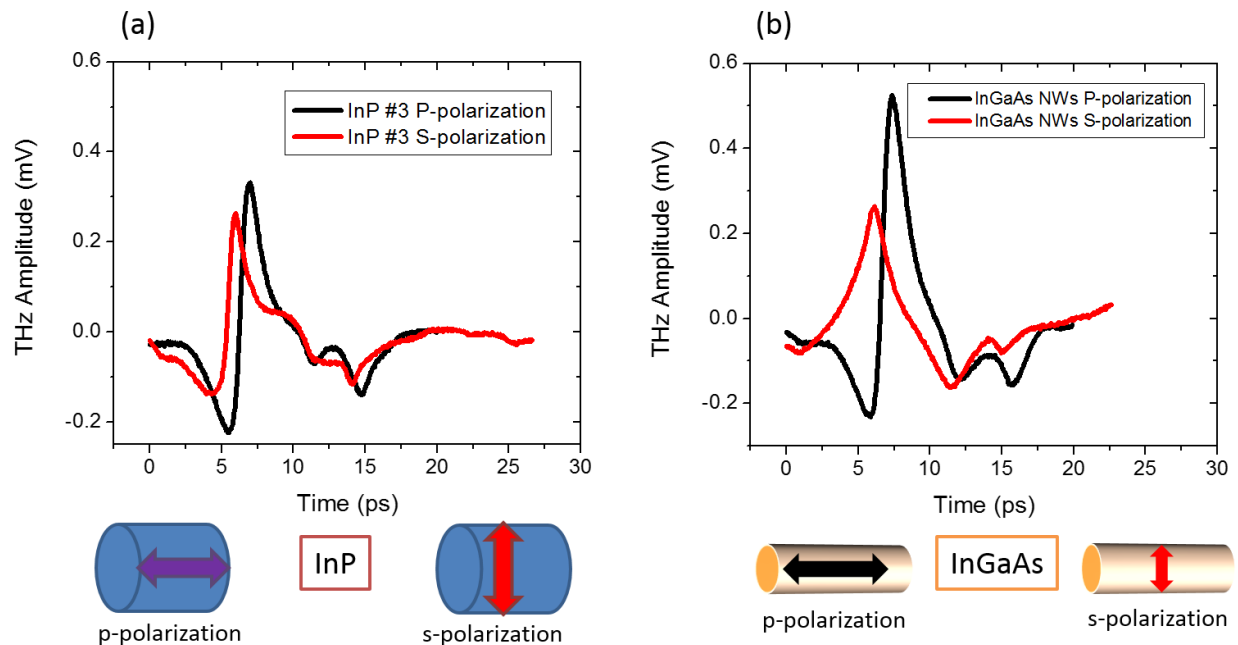


Figure 5.6 Polarization dependent measurement. THz emission from fabricated (a) InP NWs and (b) InGaAs NWs when excited by two different linearly polarized femtosecond laser pulse.

#### 5.4. Summary

In summary, we verified the THz radiation ability of SiGe NWs based on the Ge composition ratio. In addition, we also verified the better functionality of NWs surface emitter rather than bulk semiconductor surface by comparing the measurement result of NWs with those of parental wafers. On one hand, we also examined the role of the laser pulse polarization on the emitted THz intensity. On the other hand, we achieved different approach technique for the NWs fabrication by applying E-beam lithography, which is way different with the conventional growing method. This achievement enhanced the efficiency of fabricating NWs in the aspect of controllability, obtaining accurate, speedy, uniform device as an output. We suggest fabricating the NWs by e-beam lithography would bring us full control on vertical alignment and uniform distribution of the NWs, which plays an essential function in THz emission. Most of all, these continuous effort to achieve THz emission from semiconductor NWs without biasing the device will make a great contribution for the future compact THz equipment in a practical way of life.

## CHAPTER 6

### CONCLUSION

As a new THz responsive device, Flexible Metamaterial Perfect Absorbers have been investigated as an application of cloaking and stealth technology. Through this study, I could learn about metamaterial that promises unlimited applications, and also how to utilize 3D printing technology. The research results have major benefits such that the functionality of the FMPAs was evaluated and found to be consistent and robust for both under the deformation and flat condition. This result could lead to future applications in stealth technology or cloaking since this FMPA showed enough robustness when it covered another object whose surface is rough and uneven. Additionally, the FMPA's resonant response is dependent on the center-to-center displacement of the Frequency Selective Surface unit cell rings. This could be exploited for future sensing applications.

As a biological application of THz wave, human breast cancer cells and normal tissue cells were investigated. This was the first measurement dealing with the living cells in our lab. Under the transmission mode of THz-TDS measurement, there were meaningful results that can contribute to discrimination of the normal cells from cancer cells. That is because normal cell showed a distinct peak at 0.4 THz, which can be exploited for cancer cell detection. Additional measurement will be needed especially for smaller dishes than the one I used to improve the consistency of measurement condition. The diameter of dish I used was 35mm, and that was quite big for micro-scale bio cells. This resulted in us to pick random position around the dish

and each measurement was performed under the uncertain density of the cells. Therefore, I expect the measurement with smaller dishes like 5mm to 10mm will improve and verify our results. Identifying the living cells and dead cells using THz-TDS and analyzing spectroscopic data was another big achievement. I strongly believe this work will be useful for further investigation on the bio-cell study.

For the better and practical THz generation device, nanowires with specific materials were investigated. This measurement required us to set up the new optical scheme, and it was one of the best opportunities to learn how to design and operate the optical system. The invisibility of THz sometimes made us crazy, but the uncertainty also let me concentrate more on the on-scene measurement. The accumulated effort made me feel professional and finally returned the pleasure of achievement when the first NWs setup got to work. NWs are the great candidate for the compact THz equipment. As all we know, the biggest problem of THz is too expensive and too large to operate in our real life due to various affiliated equipment. In that point of view, nanowires surface emitter will finally replace all these huge equipment in a few decade. I hope our new trial of etching the NWs, instead of growing, also make a great breakthrough for the THz radiation using NWs.

## REFERENCES

- [1] I. X. Zhang, J. Xu, Introduction to THz wave photonics. Springer Publishing Company, Incorporated, 2010.
- [2] B. Ferguson, X. Zhang, "Materials for terahertz science and technology," *Nature Mater.* 1, 26-33 (2002).
- [3] P. Shumyatsky and R. R. Alfano, "Terahertz sources," *Journ of Biomedical Optics* 16 (3) 033001 (2011).
- [4] E. F. Nichols, J. D. Tear, "Short Electric Waves," *Phys. Rev.* 21, 587-610 (1923).
- [5] Zomega Terahertz Corporation, "The Terahertz Wave eBook," (2012)
- [6] J. B. Jackson, M. Mourou, J. F. Whitaker, I. N. Duling III, S. L. Williamson, M. Menu, G. A. Mourou, "Terahertz imaging for nondestructive evaluation of mural paintings," *Opt. Commun.* 281, 527-532 (2008).
- [7] DOE-NSF-NIH Workshop on "Opportunities in THz Science", Arlington, VA, February 12-14, 2004.
- [8] P.H. Siegel, "Terahertz technology," *IEEE Trans. Microw. Theory Tech.* 50, no. 3, 910-918 (2002).
- [9] P.H. Siegel, "Terahertz technology in biology and medicine," *IEEE Trans. Microw. Theory Tech.* 52, no. 10, 2438-2447 (2004).
- [10] L. Duvillaret, F. Garet, J.-L. Coutaz, "A reliable method for extraction of material parameters in terahertz time-domain spectroscopy", *IEEE J. of Selec. Top. In Quant. Electro.* 2, no. 3, 739-746 (1996).
- [11] L. Duvillaret, F. Garet, J.-L. Coutaz, "Highly Precise Determination of Optical Constants and Sample Thickness in Terahertz Time-Domain Spectroscopy," *Appl. Opt.* 38, 409-415 (1999).
- [12] F. Wang, J. Shan, E. Knoesel, M. Bonn, T. F. Heinz, "Electronic charge transport in sapphire studied by optical pump THz probe spectroscopy," *Proc. SPIE* 5352, no. 216 (2004).
- [13] T. D. Dorney, R. G. Baraniuk, D. M. Mittleman, "Material parameter estimation with terahertz time-domain spectroscopy," *J. Opt. Soc. Am. A* 18, 1562-1571 (2001).

- [14] N. Laman, S. Harsha, D. Grischikowsky, J. Mellinger, “High Resolution Waveguide THz Spectroscopy of Biological Molecules,” *Biophys. J.* 94, 1010-1020 (2008).
- [15] J. Federici and L. Moeller, “Review of terahertz and subterahertz wireless communications,” *J. Appl. Phys.* 107, 111101 (1-22) (2010).
- [16] A. Rostami, H. Rasooli, H. Baghban, *Terahertz Technology: Fundamentals and Applications*, Springer Publishing Company, Incorporated, 2011.
- [17] B. Ferguson, X.-C. Zhang, “Materials for terahertz science and technology,” *Nature Mater.* 1, 26-33 (2002).
- [18] D. H. Auston, K. P. Cheung, J. A. Valdmanis, D. A. Kleinman, “Cherenkov radiation from femtosecond optical pulses in electro-optic media,” *Phys. Rev. Lett.* 53, no. 16, 1555-1558 (1984).
- [19] N. Katzenellenbogen, D. Grischkowsky, “Efficient generation of 380 fs pulses of THz radiation by ultrafast laser pulse excitation of a biased metal semiconductor interface,” *Appl. Phys. Lett.* 58, no. 3, 222–224 (1991).
- [20] B. B. Hu, X.-C. Zhang, D. H. Auston, P. R. Smith, “Free-space radiation from electrooptic crystals,” *Appl. Phys. Lett.* 56, no. 6, 506–508 (1990).
- [21] Ch. Fattering, D. Grischkowsky, “Terahertz beams,” *Appl. Phys. Lett.* 54, no. 6, 490–492 (1989).
- [22] P. Shumyatsky, R. R. Alfano, “Terahertz sources,” *J. Biomed. Opt.* 16, no. 3 (2011).
- [23] P. R. Smith, D. H. Auston, M. C. Nuss, “Subpicosecond photoconducting dipole antennas,” *IEEE J. Quantum Electron.* 24, no. 2, 255–260 (1988).
- [24] T. A. Liu, R. H. Chou, C. L. Pan, “Dependence of terahertz radiation on gap sizes of biased multi-energy arsenic-ion-implanted and semi-insulating GaAs antennas,” *App. Phys. B* 95, 739-744 (2008).
- [25] J. T. Darrow, X. Zhang, D. H. Auston, “Saturation properties of large-aperture photoconducting antennas,” *IEEE J. Of Quantum Elec.* 28, no. 6, 1607-1616 (1992).
- [26] P. K. Benicewicz, J. P. Roberts, A. J. Taylor, “Scaling of terahertz radiation from large-aperture biased photoconductors,” *J. Opt. Soc. Am. B* 11, no. 12 (1994).
- [27] J. H. Kim, A. Polley, S. E. Ralph, “Efficient photoconductive terahertz source using line excitation,” *Opt. Lett.* 30, no. 18, 2490-2492 (2005).
- [28] M. Tani, S. Matsuura, K. Sakai, S. Nakashima, “Emission characteristics of photoconductive antennas based on low-temperature-grown GaAs and semi-insulating GaAs.” *Appl. Opt.* 36, no. 30 (1997).

- [29] M. Suzuki, H. Ohtake, T. Hirosumi, K. Fujii, M. Tonouchi, "Terahertz emissions from semiconductors excited by femtosecond pulses at wavelengths of 1560, 1050, and 780nm." *Conf. Lasers and Electro-Optics, JTuD25*. (OSA, 2006).
- [30] D. H. Auston, M. C. Nuss, "Electrooptic generation and detection of femtosecond electrical transients," *IEEE Journ. Quant. Electron.* 24, no. 2 (1988).
- [31] J. T. Darrow, B. B. Hu, X.-C. Zhang, D. H. Auston, "Subpicosecond electromagnetic pulses from large-aperture photoconducting antennas," *Opt. Lett.* 15, no. 6, 323-325 (1990).
- [32] A. G. Davies, E. H. Linfield, M. B. Johnston, "The development of terahertz sources and their applications," *Phys. Med. Biol.* 47, 3679-3689 (2002).
- [33] N. van der Valk, T. Wenckebach, P. Planken, "Full mathematical description of electro-optic detection in optically isotropic crystals," *J. Opt. Soc. of Am. B* 21, no. 3 (2004).
- [34] K. Reimann, R. P. Smith, A. M. Weiner, T. Elsaesser, and M. Woerner, "Direct field-resolved detection of terahertz transient with amplitudes of megavolts per centimeter," *Opt. Lett.* 28, 6, 471-473 (2003)
- [35] X.-C. Zhang, and D. H. Auston, "Optoelectronic measurement of semiconductor surfaces and interfaces with femtoseconds optics," *J. p. Phys.* 71, 1, 326-338 (1992)
- [36] B. Ferguson, X. -C. Zhang, "Materials for terahertz science and technology," *Nature Mater.* 1, 26-33 (2002).
- [37] Bass et al., "Optical rectification," *Phys. Rev. Lett.* 9, 446 (1962)
- [38] B. B. Hu, X. -C. Zhang, D. H. Auston, and P. R. Smith, "Free-space radiation from electrooptic crystals," *Appl. Phys. Lett.* 56 (6), 506-508 (1990).
- [39] P. R. Smith, D. H. Auston, and M. C. Nuss, "Subpicosecond photoconducting dipole antennas," *IEEE J. Quantum Electron.* 24 (2), 255-260 (1988).
- [40] Ch. Fattering and D. Grischkowsky, "Terahertz beams," *Appl. Phys. Lett.* 54 (6), 490-492 (1989).
- [41] N. Katzenellenbogen, and D. Grischkowsky, "Efficient generation of 380 fs pulses of THz radiation by ultrafast laser pulse excitation of a biased metal semiconductor interface," *Appl. Phys. Lett.* 58 (3), 222-224 (1991).
- [42] C. Kübler, R. Huber, and A. Leitenstorfer, "Ultrabroadband terahertz pulses: generation and field-resolved detection," *Semicond. Sci. Technol.* 20, S128-S133 (2005).
- [43] Coherent Laser Group, "Operator's Manual for The Coherent Mira Model 900-B Laser"

- [44] National Instruments white paper available at: <http://www.ni.com/white-paper/4541/en/> published July 28, 2011.
- [45] David. S. Wilber, “Terahertz Metamaterials for Sensing and Detection”, Ph.D dissertation, The University of Alabama (2014)
- [46] William E. Baughman, “Terahertz Spectroscopic Imaging”, M.S. Thesis, The University of Alabam (2014)
- [47] Babatunde Ajilore, “Software Implementation of Terahertz Imaging and Spectroscopy Platform”, M.S. Thesis, The University of Alabama (2010)
- [48] J. B. Pendry, A. J. Holden, D. J. Robbins, and W. J. Stewart, “Magnetism from conductors and enhanced nonlinear phenomena,” *IEEE Trans. Microwave Theory Tech.* 47 (11), 2075-2084 (1999).
- [49] N. Liu, and H. Giessen, “Coupling effects in optical metamaterials,” *Angew. Chem. Int. Ed.* 49, 9838-9852 (2010).
- [50] J. Wang, S. Qu, Z. Xu, J. Zhang, Y. Yang, H. Ma, and C. Gu, “A candidate three-dimensional GHz left-handed metamaterial composed of coplanar magnetic and electric resonators,” *Photon Nanostruct. Fundam. Appl.* 6, 183 (2008).
- [51] V. Crnojevic-Bengin, V. Radonic, and B. Jokanovic, “Fractal geometries of complementary split-ring resonators,” *IEEE Trans. Microw. Theory Tech.* 56, 10, 2312–2321 (2008).
- [52] F. Martín, F. Falcone, J. Bonache, R. Marqués, and M. Sorolla, “Miniaturized coplanar waveguide stop band filters based on multiple tuned split ring resonators,” *IEEE Microw. Wireless Compon. Lett.* 13 (12) 511-513 (2003).
- [53] J. García-García, F. Martín, F. Falcone, J. Bonache, I. Gil, T. Lopetegi, M. A. G. Laso, M. Sorolla, and R. Marqués, “Spurious passband suppression in microstrip coupled line band pass filters by means of split ring resonators,” *IEEE Microw. Wireless Compon. Lett.* 14 (9) 416-418 (2004).
- [54] H. –T. Chen, S. Palit, T. Tyler, C. M. Bingham, J. M. O. Zide, J. F. O’Hara, D. R. Smith, A. C. Gossard, R. D. Aeritt, W. J. Padilla, N. M. Jokerst, and A. J. Taylor, “Hybrid metamaterials enable fast electrical modulation of freely propagation terahertz waves,” *Appl. Phys. Lett.* 93, 091117 (1-3) (2008).
- [55] H. –T. Chen, W. J. Padilla, M. J. Cich, A. K. Azad, R. R. Averitt, and A. J. Taylor, “A metamaterial solid-state terahertz phase modulator,” *Nature Photonics* 3, 148-151 (2009).
- [56] S. A. Cummer, B. -I. Popa, D. Schurig, D. R. Smith and J. B. Pendry, “Full-wave simulations of electromagnetic cloaking structures,” *Phys. Rev. E* 74, 036621 (1-5) (2006).

- [57] D. Schurig, J. J. Mock, B. J. Justice, S. A. Cummer, J. B. Pendry, A. F. Starr, and D. R. Smith, "Metamaterial electromagnetic cloak at microwave frequencies," *Science* 314, 977-980 (2006).
- [58] N. Fang and X. Zhang, "Imaging properties of a metamaterial superlens," *Appl. Phys. Lett.* 82 (2), 161-163 (2003).
- [59] K. Aydin, I. Bulu, and E. Ozbay, "Subwavelength resolution with a negative-index metamaterial superlens," *Appl. Phys. Lett.* 90, 254102 (1-3) (2007).
- [60] H. Tao, N. I. Landy, C. M. Bingham, X. Zhang, R. D. Averitt, and W. J. Padilla, "A metamaterial absorber for terahertz regime: Design, fabrication and characterization," *Optics Express* 16 (10), 7181-7188 (2008).
- [61] K. Gilleo, "The circuit centennial," *ET-Trends* (2003).
- [62] H. Tao, A. C. Strikwerda, K. Fan, C. M. Bingham, W. J. Padilla, X. Zhang, and R. D. Averitt, "Terahertz metamaterials on free-standing highly-flexible polyimide substrates," *J. Phys. D, Appl. Phys.* 41 (23), 232004 (1-5) (2008).
- [63] J. Li, W. Withayachumnankul, S. Chang, and D. Abbott, "Metamaterial-based strain sensors," *Proc. ISSNIP*, 6146571, 30-32 (2011).
- [64] D. -H. Kim, D. -S. Kim, S. Hwang, and J. -H. Jang, "Surface relief structures for a flexible broadband terahertz absorber," *Optics Express* 20 (15), 16815-16822 (2012).
- [65] Lambert M. Surhone, Miriam T. Timpledon, Susan F. Marseken, "Radar-absorbent Material," VDM Publishing, (2010)
- [66] W. Baughman, D.S. Wilbert, S. Balci, M. Bolus, P. Kung, and S.M. Kim, "Application of terahertz spectral imaging for the identification of osseous tissue," *Proceedings of 36th International Conference on Infrared, Millimeter and Terahertz Waves (IRMMW-THz)* (2011)
- [67] DOE-NSF-NIH Workshop on "Opportunities in THz Science", Arlington, VA, February 12-14, (2004).
- [68] P.H. Siegel, "Terahertz technology in biology and medicine," *IEEE Trans. Microw. Theory Tech.*, vol. 52, no. 10, pp. 2438-2447, (2004)
- [69] P.H. Siegel, "Terahertz technology," *IEEE Trans. Microw. Theory Tech.*, vol. 50, no. 3, pp. 910-918, (2002).
- [70] X. Zhang, "Terahertz technology and applications," *SPIE Photonics West short course*, San Jose, CA., (2005).

- [71] D.L. Woolard, E.R. Brown, A.C. Samuels, J.O. Jensen, T. Globus, B. Gelmont, and M. Wolski, "Terahertz-frequency remote-sensing of biological warfare agents," *Microwave Symposium Digest, 2003 IEEE MTT-S International*, vol. 2, no. 763, (2003).
- [72] J.S. Melinger, N. Laman, and D. Grischkowsky, "The underlying terahertz vibrational spectrum of explosive solids," *Appl. Phys. Lett.*, vol. 93, no. 011102, (2008).
- [73] B. B. Hu and M. C. Nuss, *Opt. Lett.* 20, 1716 (1995)
- [74] D.M. Mittleman, R. H. Jacobsen, and M.C. Nuss, *IEEE J. Sel. Top. Quantum Electron.* 2, 679 (1996)
- [75] D. Auston, "Picosecond optoelectronic switching and gating in silicon," *Appl. Phys. Lett.* vol. 26, p. 101 (1975).
- [76] X.C. Zhang, B. B. Hu, J. T. Darrow, and D. H. Auston, "Generation of femtosecond electromagnetic pulses from semiconductor surfaces," *Appl. Phys. Lett.* vol. 56, p. 1011 (1990).
- [77] P. C. Ashworth, E. Pickwell-MacPherson, E. Provenzano, S. E. Pinder, A.D. Purushotham, M. Pepper and V. P. Wallace, "Terahertz pulsed spectroscopy of freshly excised human breast cancer," *Optical Express*, vol. 17, pp. 12444 -12454, (2009)
- [78] D. Auston, "Picosecond optoelectronic switching and gating in silicon," *Appl. Phys. Lett.* vol. 26, p. 101, (1975).
- [79] X.C. Zhang, B. B. Hu, J. T. Darrow, and D. H. Auston, "Generation of femtosecond electromagnetic pulses from semiconductor surfaces," *Appl. Phys. Lett.* vol. 56, p. 1011, (1990).
- [80] W.-J. Lee, J. W. Ma, J.M. Bae, K.-S. Jeong, M.-H. Cho, C. Kang, and J.-S. Wo, "Strongly Enhanced THz Emission caused by Localized Surface Charges in Semiconducting Germanium Nanowires," *Scientific Reports*, vol. 3, 1984, (2013)